

# Enhancing photoluminescence quantum efficiency of metal halide perovskites by examining luminescence-limiting factors

Cite as: APL Mater. **8**, 020904 (2020); <https://doi.org/10.1063/1.5136308>

Submitted: 12 November 2019 . Accepted: 14 January 2020 . Published Online: 13 February 2020

 Hyun Myung Jang,  Joo-Sung Kim,  Jung-Min Heo, and  Tae-Woo Lee



View Online



Export Citation



CrossMark

## ARTICLES YOU MAY BE INTERESTED IN

[Performance boosting strategy for perovskite light-emitting diodes](#)

Applied Physics Reviews **6**, 031402 (2019); <https://doi.org/10.1063/1.5098871>

[Metal halide perovskites for blue light emitting materials](#)

APL Materials **8**, 040907 (2020); <https://doi.org/10.1063/1.5144101>

[Polymer-perovskite blend light-emitting diodes using a self-compensated heavily doped polymeric anode](#)

APL Materials **8**, 021101 (2020); <https://doi.org/10.1063/1.5140519>

## Hall Effect Measurement Handbook

**A comprehensive resource for researchers**

Explore theory, methods, sources of errors, and ways to minimize the effects of errors



# Enhancing photoluminescence quantum efficiency of metal halide perovskites by examining luminescence-limiting factors

Cite as: APL Mater. 8, 020904 (2020); doi: 10.1063/1.5136308  
Submitted: 12 November 2019 • Accepted: 14 January 2020 •  
Published Online: 12 February 2020



Hyun Myung Jang,<sup>1,a)</sup>  Joo-Sung Kim,<sup>2</sup>  Jung-Min Heo,<sup>2</sup>  and Tae-Woo Lee<sup>1,2,3,b)</sup> 

## AFFILIATIONS

<sup>1</sup>Research Institute of Advanced Materials, Seoul National University, 1 Gwanak-ro, Gwanak-gu, Seoul 08826, South Korea

<sup>2</sup>Department of Materials Science and Engineering, BK 21 PLUS SNU Materials Division for Educating Creative Global Leaders, Seoul National University, 1 Gwanak-ro, Gwanak-gu, Seoul 08826, South Korea

<sup>3</sup>Institute of Engineering Research, Nano Systems Institute (NSI), Seoul National University, 1 Gwanak-ro, Gwanak-gu, Seoul 08826, South Korea

<sup>a)</sup>E-mail: [jang0227@snu.ac.kr](mailto:jang0227@snu.ac.kr)

<sup>b)</sup>Author to whom correspondence should be addressed: [twlees@snu.ac.kr](mailto:twlees@snu.ac.kr)

## ABSTRACT

Metal halide perovskites (MHPs) show superior optoelectronic properties, which give them the great potential for use in next generation light-emitting diodes (LEDs). In particular, their narrow emission linewidths can achieve ultrahigh color purity. However, the reported luminescence efficiency (LE) values are not high enough to be commercialized in displays and solid-state lightings. Moreover, the operational stability of LEDs associated with the overshooting of luminance and the high relative standard deviation of reported external quantum efficiencies are still problematic. In this perspective, we review photophysical factors that limit the photoluminescence quantum efficiency of perovskite-based LEDs. These factors are categorized into (i) weak exciton binding, (ii) nonradiative recombinations, (iii) slow cooling of long-lived hot carriers, (iv) deep-level defects, and (v) interband transition rates. We then present various physicochemical methods to effectively overcome these luminescence-limiting factors. We finally suggest some useful research directions to further improve the LE of MHP emitters as core components in displays and solid-state lightings.

© 2020 Author(s). All article content, except where otherwise noted, is licensed under a Creative Commons Attribution (CC BY) license (<http://creativecommons.org/licenses/by/4.0/>). <https://doi.org/10.1063/1.5136308>

## I. INTRODUCTION

Metal halide perovskites (MHPs) are promising semiconducting materials for next generation optoelectronic devices. MHPs show superior electrical and optical properties, which give them great potential for use in light-emitting diodes (LEDs).<sup>1–4</sup> In particular, their narrow emission linewidths [with a full width at half-maximum (FWHM) of  $\leq 20$  nm] can achieve ultrahigh color purity (color gamut  $\geq 140\%$  in NTSC standard). These are superior to the properties of organic emitters (FWHM  $> 40$  nm; color gamut  $< 100\%$  in NTSC standard) and inorganic quantum dot (QD) emitters (FWHM  $\approx 30$ – $40$  nm; color gamut  $\approx 120\%$  in NTSC standard).<sup>5</sup> Three-dimensional (3D) polycrystalline MHPs have  $ABX_3$ -type crystal structure, where A is an organic or inorganic cation

that functions as a structural template, B is a metal cation, and X is a halide anion.<sup>6,7</sup> Each B-site atom is surrounded by six X atoms, and each A-site cation or molecule is positioned in the center of  $BX_6$  octahedral frameworks. To be structurally stable, polycrystalline MHPs should have the tolerance factor,  $t = \frac{(r_A + r_X)}{\sqrt{2}(r_B + r_X)}$ , where  $r$  is the ionic radius, in the range  $0.8 \leq t \leq 1.0$ , and the octahedral factor ( $\mu = r_B/r_X$ ) in the range  $0.44 \leq \mu \leq 0.9$ .<sup>7–9</sup>

3D polycrystalline MHPs were first chosen for use in light emitters for perovskite-based LEDs (PeLEDs) because of the advantages of simple synthesis, easy film fabrication, and effective charge-transporting properties.<sup>2–4,10</sup> In 2014, the bright PeLEDs with a brightness of  $\sim 400$  cd/m<sup>2</sup> at room temperature had been developed using 3D polycrystalline MAPbX<sub>3</sub>-based MHP emitters by adopting

simple planar structures,<sup>2,3</sup> where MA denotes a CH<sub>3</sub>NH<sub>3</sub> organic cation. These PeLEDs had solution-processed MHP emitting layers between charge-transporting organic layers with electrodes.<sup>2,3</sup> The electroluminescence efficiencies of the early-stage PeLEDs in 2014 are (i) infrared (IR) radiance of 13.2 W/(sr m<sup>2</sup>) and external quantum efficiency (EQE) of 0.76% for MAPbI<sub>3-x</sub>Cl<sub>x</sub> and (ii) luminance  $L = 417$  cd/m<sup>2</sup> and EQE of 0.125% for MAPbBr<sub>3</sub>.<sup>2,3</sup> These are inferior to those of conventional organic light-emitting diodes (OLEDs) and lag far behind the commercially required performance. However, those solution-processed PeLEDs clearly proved the possibility of room-temperature processed next-generation LEDs with a high color purity of a narrow FWHM of  $\approx 20$  nm<sup>2,3</sup> and flexible LED devices.<sup>3</sup> The first efficient PeLEDs with EQE of 8.53% (42.9 cdA<sup>-1</sup>) similar to the level of OLEDs have been reported by making small nanograin films using additive-based nano-crystal pinning processes in 2015.<sup>4</sup> Since then, EQEs of PeLEDs have further been improved to demonstrate that PeLEDs are promising next-generation LEDs.<sup>4,11-15</sup>

Recently achieved EQEs of  $\sim 20\%$  clearly show the possibility of 3D MHPs as next-generation light emitters.<sup>16-19</sup> An island/lid-stacked structure (termed quasi-core/shell) of polycrystalline CsPbBr<sub>3</sub> capped with MABr additive yielded EQE of  $\sim 20\%$  [current efficiency (CE) = 65 cd/A] in green polycrystalline PeLED.<sup>16</sup> This structure allowed a high photoluminescence quantum yield (PLQY). An increase in light extraction efficiency in polycrystalline PeLEDs based on submicrometer-scale FAPbI<sub>3</sub> (FA = formamidinium) yielded the maximum EQE of 20.7% (the minimum EQE of 17.75% and average EQE of 19.2% with the relative standard deviation of 4%) with invisible IR emission.<sup>17</sup> The increase in light extraction from FAPbI<sub>3</sub> was achieved using an insulating layer of 5-aminovaleric acid (5AVA) to reduce leakage current through the uncovered emitter region and to passivate surface defects.<sup>17</sup> These rapid developments of PeLEDs have confirmed their possibility of utility as the next-generation emitters. However, the reported luminescence efficiency (LE) values are still lower than those of OLEDs that are commercialized in displays and solid-state lightings. Moreover, the high relative standard deviation of the reported EQEs is problematic. Therefore, it is of great importance to develop a reliable method of producing high-efficiency PeLEDs with a narrow EQE distribution.

In this perspective, we review photophysical factors that strongly affect the photoluminescence quantum efficiency (PLQE) of MHP-based PeLEDs. These factors are classified as (i) weak exciton binding in MHPs, (ii) nonradiative recombination of charge carriers, (iii) slow cooling of long-lived hot carriers, (iv) deep-level defects and ion migration, and (v) interband transition rates. By theoretically examining these points, we present various physico-chemical methods to overcome the luminescence-limiting factors and finally suggest several research directions to further improve the LE of MHP emitters as core components in displays and solid-state lightings.

## II. LUMINESCENCE-LIMITING PHYSICAL FACTORS

### A. Weak exciton binding in MHPs

The electroluminescence (EL) efficiency of PeLED is most strongly affected by charge-carrier recombination processes and

concomitant photoluminescence quantum efficiency (PLQE) of MHP emitters. Charge-carrier recombination in MHP emitters occurs in several steps [Fig. 1(a)]: Photo-illumination does excite the electrons from the valence band maximum (VBM) into conduction band minimum (CBM) and, subsequently, form electron-hole pairs, excitons (process 1). Some of these pairs recombine with each other and emit light, called "radiative recombination of electron-hole ( $e-h$ ) pairs" or "unimolecular excitonic recombination" (process 2.1). Other pairs separate into free-charge carriers (process 2.2).

Excited electrons and holes can experience an energetically stabilizing Coulombic attraction, forming electrostatically neutral quasi-particles, called excitons.<sup>20</sup> The ratio of the radiative recombination of  $e-h$  pairs to the separation into free-charge carriers (defined as  $R_{REC}$ ) is determined by the exciton binding energy ( $E_b$ ) which defines the energy needed to separate the bound  $e-h$  pairs,<sup>20</sup>

$$E_b = \frac{\mu}{2\hbar^2} \left( \frac{e^2}{4\pi\epsilon_0\epsilon_r} \right)^2 = R_H \frac{\mu}{m_0\epsilon_r^2} = \frac{e^2}{8\pi\epsilon_0\epsilon_r a_B}, \quad (1)$$

where  $R_H (=13.6$  eV) is called the Rydberg constant and denotes the binding energy of electron in the ground-state  $1s$  orbital of the hydrogen (H) atom;  $m_0$  is the mass of a free electron;  $\mu \left[ \equiv \left( \frac{1}{m_e} + \frac{1}{m_h} \right)^{-1} \right]$  is the reduced mass of charge carriers, where  $m_e$  and  $m_h$ , respectively, denote the effective mass of an electron and that of a hole; and  $\epsilon_r$  is the relative dielectric permittivity of MHPs. The  $a_B$  term in the last expression of Eq. (1) denotes the exciton Bohr radius ( $=4\pi\epsilon_0\epsilon_r\hbar^2/\mu e^2$ ) and roughly represents the average distance between the electron and the hole in a given exciton ( $e-h$  pair).

MHPs have low and similar effective masses ( $m_e \approx 0.15m_0$ ;  $m_h \approx 0.14m_0$ ) and are ion-bonded crystals, so electrons and holes can freely move, rotate, and oscillate in the MHP crystals. As a result, the reduced mass of an  $e-h$  pair is as small as  $0.072m_0$ , as obtained by  $\mu \equiv m_e m_h (m_e + m_h)^{-1}$ . On the other hand, heavy-metal atoms (e.g., Pb) and orientational motion of the A-site organic cations<sup>21</sup> in MHPs prevent the movement of charge carriers and induce screened Coulomb interaction, thereby leading to large  $\epsilon_r$  and polarization. Since  $E_b$  is proportional to  $\mu$  but is inversely proportional to the square of  $\epsilon_r$  [Eq. (1)], the observed small exciton binding energy of MHPs is mainly caused by small reduced mass ( $\mu$ ) and large dielectric permittivity ( $\epsilon_r$ ). As a result,  $E_b$  values of 3D MHPs are significantly smaller than 100 meV, 30–50 meV in MAPbI<sub>3</sub> and  $\sim 76$  meV in MAPbBr<sub>3</sub>,<sup>22,23</sup> similar to the thermal energy per atom at room temperature ( $k_B T = 25.7$  meV). These  $E_b$  values were obtained by various experimental methods, including magneto-optical absorption spectroscopy,<sup>22</sup> optical absorption,<sup>24</sup> and temperature-dependent PL.<sup>25</sup> In MHPs,  $R_{REC}$  can be estimated by applying the Saha–Langmuir equation,<sup>26</sup>

$$\frac{n \cdot x^2}{1 - x} = \frac{n_{FC}^2}{n_{exc}} = \left( \frac{2\pi\mu k_B T}{h^2} \right)^{3/2} e^{-E_b/k_B T}, \quad (2)$$

where  $n_{exc}$  denotes the density of  $e-h$  exciton pairs,  $n_{FC}$  is the density of free-charge carriers,  $x$  denotes the fraction of free carriers over the total density of exciton ( $=n_{FC}/n$ ),  $\mu$  is the reduced mass of the exciton, and  $n$  is the total density of excitation ( $=n_{FC} + n_{exc}$ ). 3D MHPs with small  $E_b$  values (30–76 meV)<sup>22,23</sup> have dominant

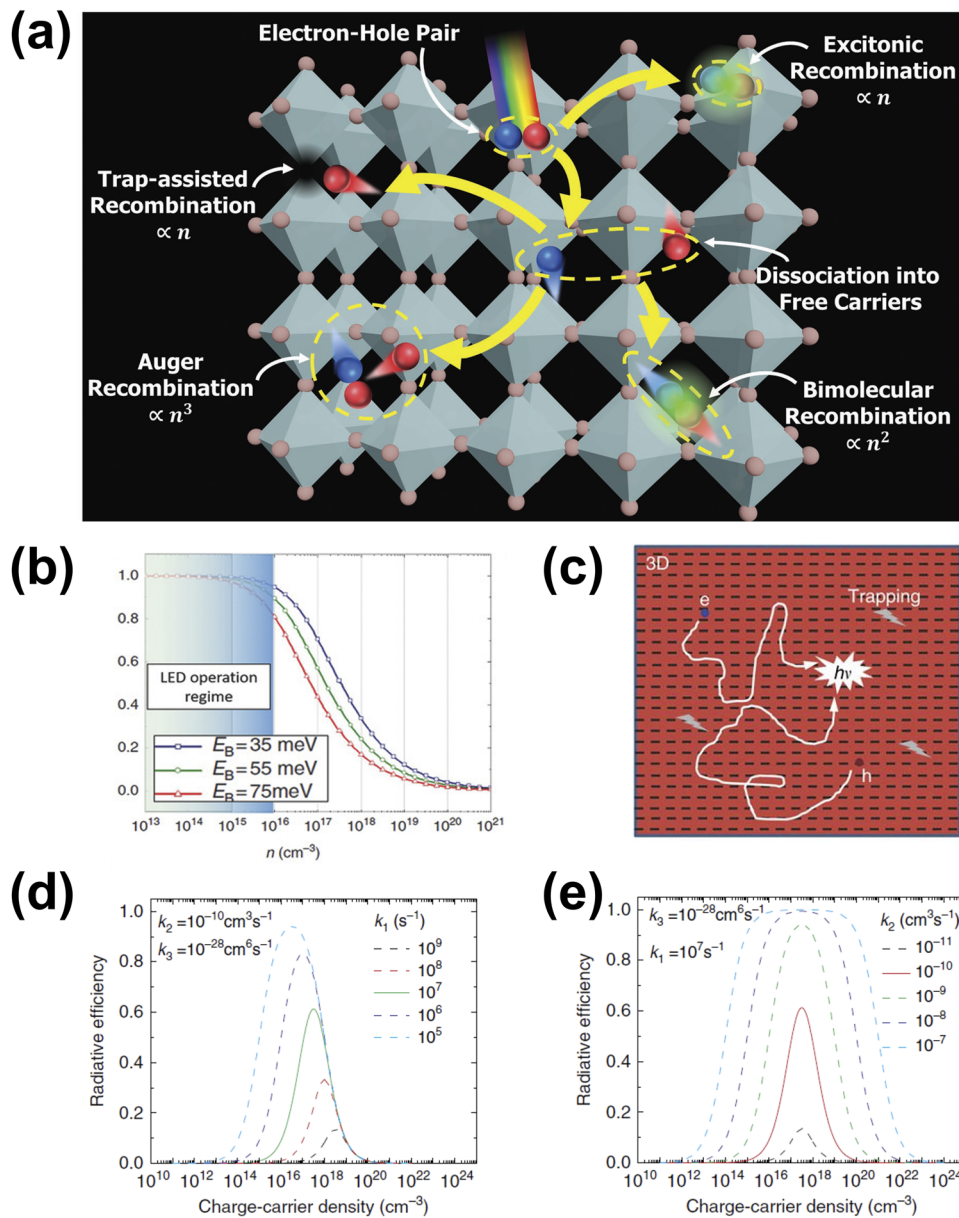


**FIG. 1.** Recombination mechanisms, kinetics, and photoluminescence efficiency of charge carriers. (a) Schematic illustration describing various recombination mechanisms of charge carriers in MHPs. The four major recombination pathways are excitonic recombination ( $\propto n^1$ ), trap-assisted recombination ( $\propto n^1$ ), bimolecular recombination ( $\propto n^2$ ), and Auger recombination ( $\propto n^3$ ). (b) The free-charge fraction ( $x$ ) plotted as a function of the total density of excitation ( $n$ ) at three different exciton binding energies. The present plot is based on Eq. (2) for the charge carriers in thermal equilibrium at room temperature. Reproduced with permission from D'Innocenzo *et al.* Nat. Commun. **5**, 3586 (2014). Copyright 2014 Nature Publishing Group. (c) Recombination pathways of excited charge carriers in 3D bulk MHPs: dissociated into free-charge carriers and then trapped in defect states or recombined to emit light. Reproduced with permission from Xing *et al.* Nat. Commun. **8**, 14558 (2017). Copyright 2017 Nature Publishing Group. (d) The calculated PLQE curves for various  $k_1$  values, all showing a peak in the PLQE at the characteristic charge-carrier density,  $(k_1/k_3)^{1/2}$ . The calculated result shows that for fixed  $k_2$  (bimolecular recombination constant) and  $k_3$  (Auger recombination constant), the PLQE increases rapidly with decreasing  $k_1$  (trap-mediated recombination constant). (e) The calculated PLQE curves for various  $k_2$  values. Since  $k_1$  and  $k_3$  are fixed, all curves exhibit their peaks at the same charge-carrier density ( $n_p$ ), namely,  $n_p = (k_1/k_3)^{1/2} = 3.16 \times 10^{17} \text{ cm}^{-3}$ . The result shows that for fixed  $k_1$  and  $k_3$  rate constants, the PLQE increases with increasing  $k_2$ . Reproduced with permission from Xing *et al.* Nat. Commun. **8**, 14558 (2017). Copyright 2017 Nature Publishing Group.

free-charge carriers at room temperature.  $R_{REC} [\equiv n_{exc}/n_{FC} = (n - n_{FC})/n_{FC}]$ , which is approximately inversely proportional to the free-charge fraction  $x (=n_{FC}/n)$ , increases gradually with increasing  $E_b$  [Fig. 1(b)] or decreasing temperature<sup>26</sup> for a given total density of excitation ( $n = n_{FC} + n_{exc}$ ). The  $n$ -dependent  $x$  shown in Fig. 1(b) follows the above Saha-Langmuir equation. This direct dissociation of electron-hole pairs into free-charge carriers has stimulated research into MHP-based solar cells but has impeded the development of MHP-based LEDs because efficient light emission in PeLEDs requires strongly bound electron-hole pairs.

One very efficient approach to overcoming this obstacle in PeLEDs is controlling the physical dimension and dimensionality of

MHPs. Decreasing the physical dimension from micrometer scale to nanometer scale in 3D perovskites greatly improves the LE of PeLEDs because reducing the particle dimension leads to the confinement of charge carriers and, consequently, enhances the rate of radiative recombination of electron-hole pairs (excitons) within a nanograin.<sup>4,13,27</sup> Similarly, strong excitonic absorption and luminescence features are observed at room temperature in layered lead halide perovskites,<sup>28</sup> with  $E_b$  values as high as  $\sim 300$  meV for typical  $n = 1$  Pb-I materials, where “ $n$ ” is the number of octahedral layers that make up a single slab in layered halide perovskites. The strong excitonic character of the layered 2D perovskites compared to their 3D congeners<sup>29</sup> results from the cooperative effects

of quantum and dielectric confinement.<sup>28</sup> Despite some differences between the layered perovskites and true quantum-well systems, these two effects, which apply to quantum wells, qualitatively explain the greatly enhanced  $E_b$  in 2D perovskites.<sup>28,30</sup>

In an electronically 3D material, such as  $(\text{CH}_3\text{NH}_3)\text{PbI}_3$ , the excitonic wavefunctions are similar to the 3D hydrogenic wavefunctions of the Bohr model.<sup>20</sup> In 2D systems, dimensional confinement of the wavefunction leads to a 4-fold enhancement of  $E_b$  relative to its 3D congener through quantum confinement.<sup>28,31</sup> On the other hand, dielectric confinement results from relatively poor screening of the Coulombic attraction between the electron and hole<sup>32,33</sup> by the organic layers that are significantly less polarizable than the inorganic layers.<sup>30</sup> The polarizability ( $\alpha_E$ ) of the halide ion seems to affect  $E_b$  as lead iodide perovskites exhibit lower  $E_b$  values than lead bromide perovskites, e.g.,  $E_b$  of  $\sim 220$  meV for  $(\text{PEA})_2\text{PbI}_4$  vs  $E_b$  of  $\sim 356$  meV for  $(\text{PEA})_2\text{PbBr}_4$ , owing to greatly enhanced  $\alpha_E$  of I, as compared with  $\alpha_E$  of Br.<sup>34,35</sup> Here, PEA stands for phenylethylene ammonium. It is now known that the reduction of both  $E_b$  (by reducing both dielectric and quantum confinements) and the bandgap ( $E_g$ ) can be achieved by increasing the thickness of the inorganic layers. The  $n = 1$  member of the  $(\text{C}_6\text{H}_5(\text{CH}_2)_2\text{NH}_3)_2(\text{CH}_3\text{NH}_3)_{n-1}\text{Pb}_n\text{I}_{3n+1}$  family [i.e.,  $(\text{PEA})_2\text{PbI}_4$ ] has  $E_g$  and  $E_b$  values of 2.58 eV and 0.220 eV, respectively, while the  $n = 2$  perovskite has corresponding values of 2.34 eV and 0.170 eV, respectively,<sup>34,36</sup> which leads to a red shifting of the luminescence with  $n$ , converging toward the emission energy of the  $n = \infty$  3D perovskite,  $(\text{CH}_3\text{NH}_3)\text{PbI}_3$ , at 1.60 eV.

## B. Nonradiative recombination processes of charge carriers

Let us now examine the recombination kinetics of charge carriers in MHPs to quantitatively address the effects of nonradiative recombination processes on the suppression of LE. Photoexcited charge carriers that separate into free charge carriers (process 2.2) can subsequently undergo one of the following three steps: bimolecular radiative recombination (process 2.2.1), or trapping into deep-level defect states, followed by the Shockley–Read–Hall (SRH) nonradiative recombination (process 2.2.2), or recombination by multiparticle interaction, and typically by three-body Auger recombination (process 2.2.3). Then, one can write the following equation for the recombination kinetics of charge carriers:<sup>37</sup>

$$\frac{dn(t)}{dt} = -k_1n - k_2n^2 - k_3n^3, \quad (3)$$

where  $n(t)$  is the charge-carrier density at time  $t$ ,  $k_2$  is the rate constant for the bimolecular recombination of free-charge carriers, and  $k_3$  denotes the rate constant for the trimolecular Auger recombination process. On the contrary, two distinct rates contribute to  $k_1$ , namely,  $k_1 = k_{1(\text{exc})} + k_{1(\text{def})}$ , where  $k_{1(\text{exc})}$  represents the rate constant for the unimolecular excitonic recombination (process 2.1) and  $k_{1(\text{def})}$  denotes the rate constant for the defect-mediated nonradiative recombination (process 2.2.2). Recombination rates of MHPs can be obtained by fitting the transient-absorption kinetics data for different pump fluences: 3D MAPbBr<sub>3</sub> films showed  $k_1 \approx 27.2 \mu\text{s}^{-1}$  (i.e.,  $27.2 \times 10^6 \text{ s}^{-1}$ ),  $k_2 \approx 4.9 \times 10^{-10} \text{ cm}^3 \text{ s}^{-1}$ , and  $k_3 \approx 13.5 \times 10^{-28} \text{ cm}^6 \text{ s}^{-1}$ , and 3D MAPbI<sub>3</sub> films showed  $k_1 \approx 72.7 \mu\text{s}^{-1}$ ,  $k_2 \approx 1.5 \times 10^{-10} \text{ cm}^3 \text{ s}^{-1}$ , and  $k_3 \approx 3.4 \times 10^{-28} \text{ cm}^6 \text{ s}^{-1}$ .<sup>38</sup> In MHPs,

$k_2$  and  $k_3$  are inherent values, whereas  $k_1$  is affected by the degree of charge-carrier confinement and by defect density. This indicates that specific recombination pathways in 3D MHPs can be controlled by tuning defect density, crystallinity, and dimensionality or physical dimension of MHP crystals.<sup>37</sup>

According to the above kinetic data, for both 3D MAPbBr<sub>3</sub> and MAPbI<sub>3</sub> films,  $k_1$  and  $k_2n$  are much greater than  $k_3n^2$  for the charge-carrier density ( $n$ ) up to  $10^{17} \text{ cm}^{-3}$ . Since a typical charge density under LED operating conditions is  $n \leq 10^{15} \text{ cm}^{-3}$ , the charge-recombination rate due to the trimolecular Auger process ( $-k_3n^3$ ) is negligible as compared with the other two contributions ( $-k_1n$  and  $-k_2n^2$ ). Under this condition, one can obtain the following solution for Eq. (3) after some mathematical manipulations:

$$n(t) = \frac{k_1 e^{-k_1 t}}{k_2 \left\{ (1 - e^{-k_1 t}) + \frac{1}{n_0} \left( \frac{k_1}{k_2} \right) \right\}}, \quad (4)$$

where  $n_0$  denotes the charge-carrier density at  $t = 0$  (initial photoexcitation density). In the initial stage of the transient PL decay,  $n(t)$  can be approximated as

$$n(t) = \frac{n_0 e^{-k_1 t}}{\{1 + k_2 n_0 t\}}. \quad (5)$$

Thus, at a low value of  $n_0$ , plotting  $\ln n(t)$  with respect to  $t$  (time after excitation) yields a single straight line with the slope being  $-k_1$  in the initial stage of decay. With increasing  $n_0$ , a linear plotting is no more valid. Instead, we have  $\frac{d \ln n(t)}{dt} = -k_1 - \frac{k_2 n_0}{\{1 + k_2 n_0 t\}}$ . Thus, the magnitude of the initial slope of PL decay (as  $t \rightarrow 0$ ) increases with increasing  $n_0$ . This prediction does accord well with the measured transient PL decay curves with different initial photoexcitation densities  $n_0$ .<sup>39</sup>

In conventional polycrystalline 3D MHPs with large grains,  $E_b$  is small, so most electron–hole pairs dissociate directly into free-charge carriers, suppressing the unimolecular excitonic recombination ( $k_1$ ) at room temperature. In view of this, the bimolecular recombination of free-charge carriers is the main radiative mechanism in conventional polycrystalline 3D MHPs with large grains at room temperature [Fig. 1(c)]. Therefore, the photoluminescence quantum yield (PLQY) or efficiency (PLQE) in MHPs can be represented as<sup>40</sup>

$$\Phi(n) = \frac{(dn/dt)_{\text{rad}}}{(dn/dt)} = \frac{k_{1(\text{exc})} + k_2n}{k_{1(\text{exc})} + k_{1(\text{def})} + k_2n + k_3n^2}, \quad (6)$$

where  $(dn/dt)_{\text{rad}}$  and  $(dn/dt)$  denote the radiative and total recombination rates, respectively. Under low excitation fluences (charge-carrier density of  $< 10^{15} \text{ cm}^{-3}$  in LED operating conditions), the defect-mediated nonradiative recombination of charge carriers [ $k_{1(\text{def})}$ ] dominates radiative recombination mechanisms, i.e., the unimolecular recombination of excitons [ $k_{1(\text{exc})}$ ] and the bimolecular recombination of free-charge carriers [ $k_2n$ ] in 3D MHP films. The PLQE then increases with increasing  $n$  due to the gradual domination of the second-order bimolecular recombination over the first-order charge-carrier trapping. At higher carrier densities, where the three-particle Auger recombination becomes effective and dominates the bimolecular recombination, the PLQE will then decrease with increasing  $n$ . This decrease in the PLQE can be attributed to a nonradiative nature of multicharge carrier interactions such as Auger and biexciton recombinations.<sup>37</sup> Since  $k_2$  ( $\sim 10^{-10} \text{ cm}^3 \text{ s}^{-1}$ )

and  $k_3$  ( $\sim 10^{-28}$  cm<sup>6</sup> s<sup>-1</sup>) are the intrinsic parameters for a given MHP,<sup>41,42</sup> one should maximize the unimolecular excitonic recombination rate [ $k_{1(exc)}$ ] for obtaining an enhanced PLQE [Eq. (6)]. This goal can be achieved either by the dimensional confinement of charge carriers using nano-sized grains in 3D MHPs<sup>4,13</sup> or by increasing the exciton binding energy ( $E_b$ ) in quantum-confined quasi-2D perovskites<sup>27,43–46</sup> (see Sec. III B). On the other hand, Eq. (6) also predicts that the trap-mediated recombination rate [ $k_{1(def)}$ ] should be minimized for achieving an enhanced PLQE.

If the bimolecular recombination rate [ $k_2$ ] is significantly higher than the recombination rate of excitons [ $k_{1(exc)}$ ], one can expect a peak in the  $n$ -dependent PLQE as the following inequality is established under this condition:<sup>37</sup>  $k_2 n^2 \gg k_{1(exc)} n \approx 0$ . Then, the peak PLQE [ $\Phi_p(n)$ ] can be obtained by imposing  $d\Phi(n)/dn = 0$  and is given by

$$\Phi_p = \frac{1}{1 + 2(k_1 k_3)^{1/2} k_2^{-1}}, \quad (7)$$

where the charge-carrier density at the peak is given by  $n_p = (k_1/k_3)^{1/2}$ . This relation is valid for the trap-mediated recombination only,<sup>37</sup> where  $k_1 \approx k_{1(def)}$ . The calculated PLQE curves for various  $k_1$  values all show a peak in the PLQE at the characteristic charge-carrier density,  $(k_1/k_3)^{1/2}$  [Fig. 1(d)]. One can immediately deduce the following important conclusions for enhancing luminescence efficiency from Eq. (7): (i) For fixed  $k_2$  and  $k_3$ , the PLQE increases rapidly with decreasing  $k_1$  [Fig. 1(d)] and (ii) for fixed  $k_1$  and  $k_3$  rate constants, the PLQE increases with increasing  $k_2$ , bimolecular recombination rate [Fig. 1(e)].<sup>37</sup> As mentioned previously,  $k_2$  and  $k_3$  are the intrinsic parameters for a given MHP.<sup>41,42</sup> Thus, one should suitably minimize the trap-mediated recombination rate [ $k_{1(def)}$ ] for obtaining an enhanced PLQE. Fortunately, the long first-order lifetimes,  $\tau_1 (= k_1^{-1}) \approx 0.1$ – $1$   $\mu$ s, are indicative of the absence of deep-level defects, which is caused by characteristic low defect-formation energies in MHPs.<sup>47–49</sup> In MHP bulk systems, lower first-order recombination rates and conversely long minority carrier lifetimes obtained from time-resolved PL ( $\tau_{avg} \approx k_1^{-1}$ ) are indicators of a low defect concentration which is desirable in both LEDs and solar cells. If the bimolecular recombination rate is not sufficiently high, the above inequality, i.e.,  $k_2 n^2 \gg k_{1(exc)} n$ , is no more valid. Under this condition, increasing  $k_{1(exc)}$  is the most effective way of obtaining high LEs of PeLEDs. As stated in the previous paragraph, this can be achieved by confining the charge carriers using nano-sized grains<sup>4,13</sup> or by increasing the exciton binding energy.<sup>27,43–46</sup>

Indirect bandgap in MHPs does slow down the recombination rate of charge carriers and limits the PLQE of MHPs.<sup>5,38,50–52</sup> Heavy B-site ions (e.g., Pb) in the MX<sub>6</sub> octahedron induce a strong spin-orbit coupling ( $\sigma \cdot \mathbf{p}$ ), where  $\sigma$  denotes the Pauli spin operator and  $\mathbf{p}$  is the linear momentum parallel to the spin-orbit coupling (Rashba) plane. This spin-orbit coupling term then vectorially couples with a gradient of the local electric potential ( $\nabla_{\perp} V$ ) which originates from non-centrosymmetry (i.e., break in the inversion symmetry). Consequently, the conduction (CB) and valence (VB) bands are spin degenerate and the band-energy curve does split in momentum space, termed the Rashba splitting, with the magnitude of  $2\Delta k = 2m\alpha/\hbar^2$ , where  $\alpha$  is the Rashba interaction coefficient. According to quantum molecular dynamics simulations,<sup>52</sup> however, the VB

Rashba splitting is significantly smaller than the corresponding CB value. This can be attributed to the different atomic-orbital contribution at the band edge:<sup>52</sup> largely asymmetric Pb  $6p + I$   $5p$  for the CBM vs less asymmetric Pb  $6s + I$   $5p$  for the VBM in MAPbI<sub>3</sub>, where CBM and VBM, respectively, denote the conduction band minimum and the valence band maximum. The Rashba splitting then results in a spin-forbidden  $e$ - $h$  recombination channel and, consequently, leads to a suppressed charge-carrier recombination rate and a longer carrier lifetime.<sup>51</sup> However, a more recent *ab initio* molecular dynamics study showed that the optical transition between the lowest CB and the highest VB is spin-allowed, and thus, the Rashba splitting does not necessarily suppress the  $e$ - $h$  recombination rate.<sup>53</sup> Besides, the orientation of organic A-site cations can also induce indirect bandgaps in MHPs.<sup>54,55</sup> This indirect bandgap is measured to be 25–75 meV below the direct bandgap in MAPbI<sub>3</sub>.<sup>55</sup>

### C. Slow cooling of long-lived hot carriers

Long-lived hot carriers can also limit the LE of MHPs for the following reasons: (i) Radiative recombination is slower in hot carriers than in charge carriers at the band edge. (ii) Energy of hot carriers can be reabsorbed in the crystals.<sup>56</sup> (iii) Hot carriers with long lifetimes can also be readily trapped by defect states and, subsequently, undergo nonradiative recombination. Slow cooling of long-lived hot carriers in MHPs is mainly attributed to the following two mechanisms: (a) formation of large polarons at low excitation densities ( $< 10^{18}$  cm<sup>-3</sup>), which is caused by the electron-phonon coupling, more specifically, by the long-range Coulomb interaction between the excess electron (hole) and the ionic lattice<sup>56–61</sup> and (b) hot-phonon bottleneck under high excitation densities ( $> 10^{18}$  cm<sup>-3</sup>).<sup>62–64</sup>

Let us briefly introduce elementary polaron physics before we examine the large polaron formation in MHPs. For strong electron-phonon coupling, typical of ionic polar solids, there are two driving forces for the polaron formation: (i) the long-range Coulomb potential ( $V^{LR}$ ) between the excess electron (hole) and the ionic lattice, i.e., electron-phonon coupling, and (ii) the short-range deformation potential ( $V^{SR}$ ) due to the change in local bonding by the excess charge.<sup>57</sup> The former is described by

$$V^{LR}(\mathbf{r}) = - \left[ \frac{1}{\epsilon_r(\infty)} - \frac{1}{\epsilon_r(0)} \right] \frac{e^2}{|\mathbf{r}| \epsilon_0}, \quad (8)$$

where  $\mathbf{r}$  is the vector between an electron and an ionic site,  $e$  is the electron charge,  $\epsilon_0$  is the permittivity of free-space, and  $\epsilon_r(0)$  and  $\epsilon_r(\infty)$  are the static and high-frequency dielectric constants, respectively. The difference between the two terms in the square bracket ensures that the fast electronic-cloud contribution to the polarizability is eliminated from  $V^{LR}$ , leaving behind only the slow nuclear contribution.  $V^{LR}(\mathbf{r})$  is insignificant when the two dielectric constants are similar,  $\epsilon_r(0) \approx \epsilon_r(\infty)$ , as is the case for crystalline Si or GaAs, and becomes important for ionic solids where  $\epsilon_r(0)$  can be more than twice the value of  $\epsilon_r(\infty)$ . Depending on whether  $V^{SR}$  or  $V^{LR}$  dominates, the result is either a small or large polaron, respectively. In the former, the size of the polarization cloud, called the coherence length ( $L_{coh}$ ), is smaller than the unit-cell dimension ( $a$ ),  $L_{coh} < a$ . In the latter case,  $L_{coh} > a$ . The difference between a small and a large polaron is not just in their size but more importantly in their transport.<sup>57</sup> The motion of small polarons occurs incoherently,

with a low mobility ( $\mu \ll 1 \text{ cm}^2 \text{ V}^{-1} \text{ s}^{-1}$ ) that increases with temperature ( $\partial\mu/\partial T > 0$ ) due to thermally activated hopping from one localized site to another. In contrast, the transport of a large polaron is coherent, and the mobility decreases with temperature ( $\partial\mu/\partial T < 0$ ). In this regard, large polaron transport resembles the coherent transport of a free electron (hole) in the conduction band.

Photoexcitation in MHPs (MAPbBr<sub>3</sub>, FAPbBr<sub>3</sub>, and CsPbBr<sub>3</sub>) with higher energy than their bandgaps at low exciton densities ( $\sim 7 \times 10^{16} \text{ cm}^{-3}$ ) does induce the formation of charge carriers at the bandgap edge and also of hot carriers. Anisotropic local reorientation motion of the organic A-site cations in organic-inorganic hybrid MHPs (e.g., MAPbBr<sub>3</sub> and FAPbBr<sub>3</sub>) induces a strong vibrational coupling between BX<sub>3</sub><sup>-</sup> and A<sup>+</sup>, leading to the formation of large polarons. A direct consequence of large polaron formation is the efficient screening of the Coulomb potential. More specifically, it screens the scattering of hot carriers with the longitudinal optical (LO) phonons (i.e., electron-phonon coupling), prevents the energetic hot carriers from cooling down, and, thus, forms hot carriers of which  $\sim 24\%$  of the PL population is long-lived ( $\sim 0.5 \text{ ns}$ ).<sup>56</sup> Time-resolved optical Kerr effect (TR-OKE) responses revealed liquid-like dynamics in MAPbBr<sub>3</sub> and FAPbBr<sub>3</sub>, but not in CsPbBr<sub>3</sub> (Fig. 2). This finding correlates well with the presence of long-lived hot carriers in the former and suggests the role of organic molecular dipole motion in energetic carrier protection.<sup>56</sup> Recently, CsPbBr<sub>3</sub> (or all-inorganic MHPs, in general) was also reported to have polarons due to soft, polarized, and flexible PbBr<sub>6</sub><sup>-4</sup> frameworks that can readily couple with charge carriers.<sup>58-61</sup> These large polarons formed by electron-phonon or vibronic coupling between excess charge carriers and highly ionized crystalline lattices are widely delocalized in crystals (over several unit cells) and can screen the scattering of hot carriers with LO phonons and, thus, remarkably reduce the cooling rate of hot carriers. In other words, once a large polaron protection shield is formed around an electron or hole, the Coulomb interaction [ $V^{LR}$ ] responsible for its scattering with LO phonons is screened, leading to a drastically reduced rate of hot-carrier cooling.<sup>56</sup> Furthermore, polarons themselves recombine much more slowly than do charge carriers.<sup>58,61</sup> Thus, the formation of large polarons can reduce the recombination rate of charge carriers and, thus, limit the LE of MHPs. One effective strategy of suppressing the formation of large polarons, thus increasing the LE, is to physically confine the size of polarons by suitably exploiting nano-sized grains in 3D MHPs, which concomitantly causes a remarkable increase in  $k_{1(exc)}$  by the exciton confinement.<sup>4,13</sup> The electron-lattice coupling strength of a large polaron (i.e., Fröhlich polaron) is given by the following unitless parameter:

$$\alpha = \frac{e^2}{\hbar c} \sqrt{\frac{m_b c^2}{2\hbar\omega_{LO}}} \left[ \frac{1}{\epsilon_r(\infty)} - \frac{1}{\epsilon_r(0)} \right], \quad (9)$$

where  $m_b$  is the effective mass given by the band structure (i.e., not adjusted for polaronic effects) and  $\omega_{LO}$  is the LO-phonon angular frequency. For  $\alpha \leq 2$  which is probably valid for MHPs, the polaron radius ( $R_p$ ) is inversely proportional to  $(\omega_{LO})^{1/2}$  and is given by

$$R_p^2 \approx \frac{2\hbar}{m_b \omega_{LO}} \left( 1 - \frac{\alpha}{6} \right). \quad (10)$$

For stronger electron-phonon coupling ( $\alpha \gg 1$ ), a different form of  $R_p$ , which is inversely proportional to  $\alpha$ , is used,  $R_p = (3\pi/2\sqrt{2}\alpha)$ .<sup>65</sup>

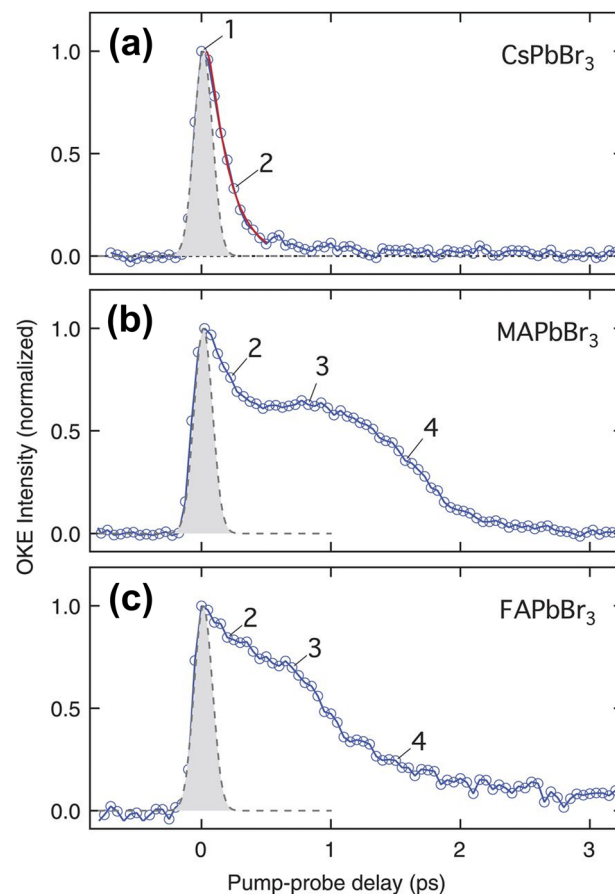


**FIG. 2.** Time-resolved optical Kerr effect (TR-OKE) responses from (a) CsPbBr<sub>3</sub>, (b) MAPbBr<sub>3</sub>, and (c) FAPbBr<sub>3</sub>. The TR-OKE transients of (b) MAPbBr<sub>3</sub> and (c) FAPbBr<sub>3</sub> [both belong to hybrid organic-inorganic perovskites (HOIP)] all show characteristic long-time responses covering a broad time window, from  $\sim 10^2$  fs to  $\sim 2$  ps. Indeed, both HOIP spectra are similar to typical TR-OKE responses from anisotropic molecular liquids, revealing liquid-like reorientational dynamics in MAPbBr<sub>3</sub> or FAPbBr<sub>3</sub>. On the contrary, the signal from CsPbBr<sub>3</sub> (a) does not show any indication of liquid-like reorientational dynamics but is characterized by (i) an instantaneous electronic response (identical to the pump-probe cross correlation, corresponding to the gray region with 70 fs full width at half-maximum) and (ii) an ultrafast response with a lifetime ( $\tau$ ) of  $140 \pm 10$  fs (red curve). This ultrafast response was attributed to fast reorientation of the local polarization anisotropy. Reproduced with permission from Zhu *et al.* *Science* **353**, 1409 (2016). Copyright 2016 The American Association for the Advancement of Science.

The parameter  $\alpha$  which is proportional to  $V^{LR}$  is roughly twice the total number of phonons in the phonon cloud ( $\alpha \approx 2N$ ) of a given electron or hole, and thus, polaronic effects are likely to be significant when  $\alpha$  becomes order-unity or larger.  $\alpha$  values of three common MHPs are 2.17 for MAPbCl<sub>3</sub>, 1.69 for MAPbBr<sub>3</sub>, and 1.72 for MAPbI<sub>3</sub>.<sup>24,66</sup> Thus, the electron-lattice coupling in MHPs is considered to be significant.

The large polaron model also explains the inverse dependence of long-lived excess electronic energy on the excitation density.<sup>56</sup> Because of the competition for nuclear polarization, there is an effective inter-polaron repulsive interaction that destabilizes large

polarons at high excitation densities. As a result of this destabilization of the large polaron protection shield (reduced screening effect), the cooling rate of energetic hot carriers by LO-phonon scattering increases with the excitation density up to the onset of a hot-phonon bottleneck ( $10^{18} \text{ cm}^{-3}$ ).<sup>56</sup> Beyond this level, the effective temperature of the more free-electron/hole-like carriers increases again with the excitation density.<sup>67</sup>

Under high excitation densities ( $>10^{18} \text{ cm}^{-3}$ ), excess hot phonons are generated, so phonon reabsorption can occur.<sup>64</sup> This process, termed hot-phonon bottleneck, slows down the cooling of hot carriers and, consequently, limits the bimolecular recombination rate ( $k_2$ ) in MHPs. This seems plausible due to the known strong coupling between electrons and the Pb-X (halide) longitudinal optical (LO) phonons<sup>68</sup> and low thermal conductivity of MHPs. Hot phonons can reheat the charge carriers and, thus, reduce the cooling rate of charge carriers.<sup>60</sup> Directly after photo-excitation by the photon energy greater than the bandgap of MHPs, the measured transient absorption spectra showed high-energy tails (at  $\sim 1.58 \text{ eV}$  in MAPbI<sub>3</sub>) and broadened spectra due to distribution and reabsorption of hot carriers over the bandgap. This is a result of reheating by the phonon bottleneck and increases the lifetime of hot carriers.<sup>63</sup> In MAPbI<sub>3</sub>, the lifetime of hot carriers gradually increases with the excitation density under the condition of high excitation density ( $>10^{18} \text{ cm}^{-3}$ ). This observation confirms that long-lived hot carriers are formed by the hot phonon-bottleneck effect rather than by the polaron effect above the critical excitation density.<sup>63</sup>

These exciton-ionic lattice interactions can be intensified in low-dimensional (e.g., 2D, 0D) perovskites in which self-assembled quantum wells (in 2D crystals) or nanocrystals (NCs; in colloidal 0D crystals) are bound by a weak van der Waals interaction.<sup>37</sup> Many dangling bonds such as out-of-plane self-terminations of PbX<sub>6</sub> octahedra (in 2D crystals) and NC surfaces (in 0D crystals), and excess charge carriers due to efficient spatial confinement perturb the lattices and cause strong charge carrier-ionic lattice interaction.<sup>37</sup> 2D MHPs [(C<sub>10</sub>H<sub>7</sub>CH<sub>2</sub>NH<sub>3</sub>)<sub>2</sub>PbI<sub>4</sub>] show a much stronger exciton-LO phonon coupling strength ( $\sim 260 \text{ meV}$ )<sup>37</sup> than 3D MHPs ( $\sim 40 \text{ meV}$  in FAPbI<sub>3</sub>,  $\sim 61 \text{ meV}$  in FAPbBr<sub>3</sub>,  $\sim 40 \text{ meV}$  in MAPbI<sub>3</sub>,  $\sim 58 \text{ meV}$  in MAPbBr<sub>3</sub>,<sup>68</sup> and  $\sim 92.1 \text{ meV}$  in MAPbI<sub>3-x</sub>Cl<sub>x</sub><sup>25</sup>). The strong electron-LO-phonon coupling may reduce the LE but more directly influence the line broadening in PL spectra which, consequently, limits the color purity of MHPs. This contribution to the PL broadening [ $\Delta\Gamma_{LO}(T)$ ] can be separately assessed by using the Bose-Einstein distribution function,

$$\Delta\Gamma_{LO}(T) = \frac{\gamma_{LO}}{\left[\exp\left(\frac{E_{LO}}{k_B T}\right) - 1\right]}, \quad (11)$$

where  $\gamma_{LO}$  denotes the exciton-LO phonon coupling strength and  $E_{LO}$  is an energy representative of the frequency for the weakly dispersive LO phonon branch.<sup>68</sup>

#### D. Deep-level defects and ion migration

As discussed in Sec. II B,  $k_2$  and  $k_3$  are inherent values in MHPs, whereas  $k_1$  is affected by the degree of charge-carrier confinement and by defect density.<sup>37</sup> Therefore, recombination pathways of charge carriers in bulk MHPs are dominantly affected by the defect density. More specifically, the PLQE of MHPs depends

strongly on the defect density because defect-mediated recombination occurs mostly by the SRH-type nonradiative mechanism and is much faster than other radiative recombination pathways [ $k_{1(def)} > k_{1(exc)}$  or  $k_2$ ].<sup>69</sup> Therefore, the SRH-type nonradiative recombination via deep-level defects may explain the observed low PLQE in MHPs [Eq. (6) or (7) for fixed  $k_2$  and  $k_3$ ]. According to first-principles defect-energy calculations,<sup>70</sup> defects with low formation energies tend to create shallow electronic levels near VBM (acceptors) or CBM (donors).<sup>48</sup> In MAPbI<sub>3</sub>, common shallow-level acceptors are  $V_{Pb}^{2-}$ ,  $I_i^{1-}$ , and  $V_{MA}^{1-}$ . On the other hand, common shallow-level donors are  $MA_i^{1+}$  and  $V_I^{1+}$  [Fig. 3]. On the contrary, defects having high formation energies create deep trap levels in the bandgap:  $I_{MA}^{2-}$ ,  $I_{Pb}^{3-}$  acceptors and  $Pb_i^{2+}$ ,  $Pb_j^{3+}$  donors (Fig. 3) in MAPbI<sub>3</sub>.<sup>48</sup> These deep-level defects act as the SRH-type nonradiative recombination centers. The nonradiative recombination rate [ $k_{1(def)}$ ] is fast as mentioned previously. However, the probability of occurrence of deep-level defects is intrinsically low (thus, minority defects) in MHPs owing to their relatively higher formation energies in MAPbI<sub>3</sub> or CSPbI<sub>3</sub>.<sup>48,71</sup> This explains the reported long electron-hole diffusion length and high open-circuit voltage  $V_{oc}$  observed in MHP-based solar cells.<sup>72</sup>

Although deep-level defects with high formation energies are thermodynamically unfavorable,<sup>48,72</sup> they can readily be incorporated into MHP crystals due to their low processing temperatures. Because MHP crystals are formed at relatively low temperatures ( $\sim 25^\circ \text{C}$  for colloidal NCs synthesized by recrystallization methods;<sup>73</sup>  $<100^\circ \text{C}$  for MHP polycrystalline bulk films;<sup>4</sup>  $<200^\circ \text{C}$  for MHP NCs synthesized by hot-injection methods<sup>74</sup>) and are held together by brittle ionic bonding, they naturally incorporate various types of defects including (i) Schottky defects that are neutral vacancy defects (e.g., PbX<sub>2</sub> vacancy and MAX vacancy), (ii) Frenkel defects that induce the charge difference in crystals (e.g., elemental defects of Pb<sup>2+</sup>, I<sup>-</sup>, and MA<sup>+</sup>, and unintentional doping), and (iii) structural defects (e.g., lattice distortion by accumulated charges and impurities at grain boundaries). Formation of defect states at surfaces or grain boundaries is accelerated because perovskite crystals are susceptible to deformation at the surface (bulk trap density of  $\sim 5 \times 10^{16} \text{ cm}^{-3}$  vs surface trap density of  $\sim 1.6 \times 10^{17} \text{ cm}^{-3}$  for MAPbI<sub>3</sub> thin films).<sup>75</sup> These defect states can also be formed by electron-phonon coupling and ion migration.<sup>76,77</sup> Schottky-type neutral defects are also readily formed (owing to low defect-formation energies around 50 meV) with their defect-energy levels located between 100 meV and 400 meV below the band edge in MHPs.<sup>77</sup> Thus, these deep-level neutral defects can trap charge carriers and, consequently, limit the LE of MHPs.

There have been recent reports on PeLEDs regarding overshooting of luminance at the initial stage of operation.<sup>17,78,79</sup> This becomes the major problem of MHPs for their applications to LEDs. However, the underlying mechanism of this phenomenon has not elucidated yet. Because a higher electric field is applied for the operation of PeLEDs as compared to the built-in voltages in perovskite-based solar cells, the ion migration tends to negatively influence the operational stability of PeLEDs. Therefore, it is necessary to suppress ion migration in PeLEDs to improve the device lifetime.<sup>77,78,80-82</sup> This is especially true for the migration on grain boundary (GB). The ion migration is widely known to occur on GB due to its highly unstable nature; thus, blocking the possible migration pathways through the GB can be an effective way to

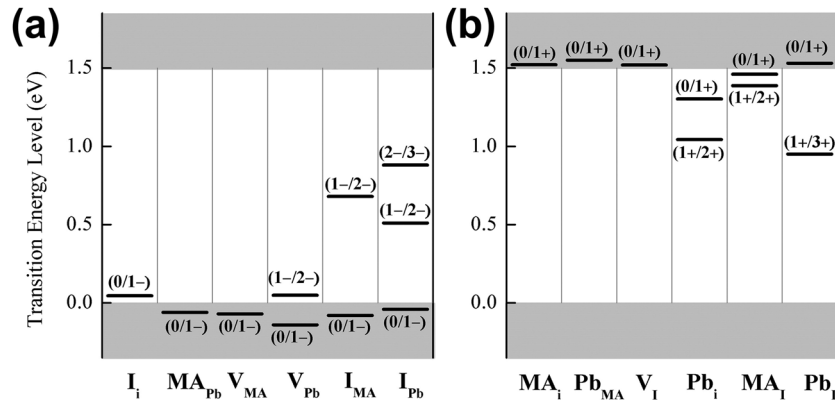


**FIG. 3.** The calculated transition energy levels of (a) intrinsic acceptors and (b) intrinsic donors in MAPbI<sub>3</sub>. Herein, the transition energy level [ $\varepsilon_\alpha(q/q')$ ] of a defect is defined as the Fermi-level position where a given defect (named  $\alpha$ ) can donate or accept electrons. For the transition between ionic states  $q$  and  $q'$ , the two corresponding defect-formation energies should be equal to each other. In other words,  $\Delta H_f(\alpha, q) = \Delta H_f(\alpha, q')$ .  $\Delta H_f$  can further be decomposed into three distinct contributions (Ref. 70): (i) the elemental-energy terms ( $\sum_i n_i E(i)$ ) with the defect-energy term [termed  $\Delta E(\alpha, q)$ ], (ii) the chemical-potential contributions of constituents ( $\sum n_i \mu_i$ ), and (iii) the electronic energy ( $qE_F$ ) referenced to the valence band maximum (VBM). Thus,  $\Delta H_f(\alpha, q) = \Delta E(\alpha, q) + \sum n_i \mu_i + qE_F$ , where  $\mu_i$  denotes the chemical potential of ionic species  $i$  and  $E_F$  designates the Fermi level. From this relation, one can immediately obtain the following expression of the transition energy level for the defect  $\alpha$ :  $\varepsilon_\alpha(q/q') = \frac{[\Delta E(\alpha, q) - \Delta E(\alpha, q')]}{(q' - q)}$ . *Ab initio* calculations are needed to estimate  $\Delta E(\alpha, q)$ , thus,  $\varepsilon_\alpha(q/q')$ . Reproduced with permission from Yin *et al.* Appl. Phys. Lett. **104**, 063903 (2014). Copyright 2014 The AIP Publishing LLC.

suppress the ion migration and to, consequently, improve the device lifetime.<sup>13,83,84</sup>

### E. Interband transition rates

Yin *et al.*<sup>72</sup> have shown that MAPbI<sub>3</sub>-based perovskites exhibit intrinsic properties that are superior for solar cell applications. These include (i) extremely high optical absorption, (ii) small effective masses for electrons and holes, and (iii) dominant point defects that only generate shallow levels, as discussed in Sec. II D. According to Fermi's golden rule, the strong optical absorption is intimately related to the strong optical emission. If the transition moment integral is assumed to be independent of  $\mathbf{k}$  (electron's wave-vector), the photon-emission rate from the conduction band can be written as<sup>85,86</sup>

$$R_{cv} = \frac{2\pi}{\hbar} \left| \int \psi_v^* \tilde{H} \psi_c d^3 r \right|^2 \cdot \int \frac{2}{8\pi^3} \delta\{E_c(\mathbf{k}) - E_v(\mathbf{k}) - \hbar\omega\} d^3 k$$

$$= \frac{2\pi}{\hbar} \frac{e^2}{m_0^2} \left\{ \frac{\hbar(n_{ph} + 1)}{2\omega\varepsilon} \right\} \left| \int \psi_v^*(\mathbf{a} \cdot \mathbf{p}) e^{-k_{ph} \cdot \mathbf{r}} \psi_c d^3 r \right|^2$$

$$\times \int \frac{2}{8\pi^3} \delta\{E_c(\mathbf{k}) - E_v(\mathbf{k}) - \hbar\omega\} d^3 k, \quad (12)$$

where  $n_{ph}$  is the photon density in the initial state,  $\psi_c$  designates the wavefunction in the (initial) conduction state,  $\mathbf{a}$  denotes the polarization unit vector which is parallel to the electric-field component of the electromagnetic (photon) wave, and the second integral involving the delta-function denotes the joint density of state (JDOS) which represents the density of optical transitions that satisfy the Planck condition. According to *ab initio* calculations,<sup>72</sup> the JDOS of MAPbI<sub>3</sub> is remarkably higher than those of prototypic GaAs and CsSnI<sub>3</sub> photovoltaics for the photon energy between 2 eV and

3.8 eV, which explains the observed strong optical absorption of MAPbI<sub>3</sub>-based perovskites in the visible energy range (1.7–3.2 eV).<sup>72</sup>

Two additional possibilities of enhancing the optical transition rate, thus, PL efficiency, can be deduced by considering the transition moment integral, i.e., the first integral, in Eq. (12),<sup>85</sup>

$$\left| \langle \mathbf{a} \cdot \mathbf{p}_{if} \rangle \right| \equiv \left| \int \psi_v^*(\mathbf{a} \cdot \mathbf{p}) e^{-k_{ph} \cdot \mathbf{r}} \psi_c d^3 r \right| \equiv \left| \int \psi_v^* \tilde{P}_a \psi_c e^{-k_{ph} \cdot \mathbf{r}} d^3 r \right|$$

$$\approx \left| \int \psi_v^* \tilde{P}_a \psi_c d^3 r \right| \equiv \langle v | \tilde{P}_a | c \rangle = m_0 \frac{d}{dt} \langle v | r | c \rangle, \quad (13)$$

where  $\tilde{P}_a$  denotes the electron's momentum operator component projected on the polarization direction, ( $=\mathbf{a} \cdot \mathbf{p}$ ). In other words, it represents the interaction of the electron momentum with the vector-field ( $\mathbf{A}$ ) component of the electromagnetic field. Thus,  $\tilde{P}_a$  is parallel to the electric-field component of the emitting electromagnetic wave (i.e.,  $\cos \theta$  between  $\mathbf{a}$  and  $\mathbf{p}$  with  $\theta = 0^\circ$ ). The fourth expression was obtained by adopting the so-called dipole approximation, namely,  $e^{-k_{ph} \cdot \mathbf{r}} = 1$ . This is fairly accurate as the wavelength of the emitting photon ( $\lambda_{ph}$ ) is much longer than the scale of the electron cloud associated with the emission (or absorption),  $\mathbf{k}_{ph} \cdot \mathbf{r} = \frac{2\pi}{\lambda_{ph}} r \approx 0$ , since  $r \ll \lambda_{ph}$  with  $\lambda_{ph} =$  order of a few hundred nanometers ( $\sim 500$  nm) and  $r =$  order of 0.1 nm.

According to the Schrödinger picture, the time-dependence of the initial (conduction) and final (valence) stationary states can be written as  $|c(t)\rangle = |c(0)\rangle e^{iE_c t/\hbar}$  and  $|v(t)\rangle = |v(0)\rangle e^{iE_v t/\hbar}$ . Using these expressions, the time-dependence of Eq. (13) can be eliminated.<sup>85</sup> Thus, the transition moment integral can be rewritten as

$$\left| \langle \mathbf{a} \cdot \mathbf{p}_{if} \rangle \right| = m_0 \frac{d}{dt} \langle v | r | c \rangle = \frac{im_0(E_c - E_v)}{\hbar} \langle v | r | c \rangle = im_0 \omega_{cv} \langle v | r | c \rangle, \quad (14)$$

where  $E_c - E_v = \hbar\omega_{cv}$ . The first point to be considered in Eq. (14) is the odd-even symmetry of the transition moment integral which is directly related to the symmetry of wavefunctions involved in a given optical transition.<sup>87</sup> In the case of MAPbI<sub>3</sub>,  $\psi_v$  is represented by the symmetric 6s orbital (+ sign) of Pb<sup>2+</sup> coupled with the I 5p\* orbital (- sign) of Pb<sup>2+</sup> coupled with the I 5p\* orbital.<sup>48,88</sup> The integral  $\langle v|r|c\rangle$  in the last expression of Eq. (14) is an even function of  $r$  since the overall symmetry is  $\langle +|-|- \rangle = +$ , where “- symmetry”, for example, denotes an odd function of  $r$ . Thus, the matrix element,  $\langle v|r|c\rangle$ , does contribute to a non-zero transition rate. Moreover, this  $c$ - $v$  emission in the tetragonal and orthorhombic phases corresponds to a direct bandgap transition at the  $\Gamma$ -point.<sup>88,89</sup> The second point of emphasis is the transition rate [ $R_{cv}$  in Eq. (12)], i.e., the transition probability per unit time, is proportional to the square of the transition dipole moment,  $|\langle v|r|c\rangle|^2$ . Thus, the PL efficiency of an emitting system which is composed of randomly oriented nanocrystals can be improved greatly if all of the transition dipole moments are aligned along a certain desired direction by employing a suitable experimental technique. Otherwise, a nanocrystalline system having randomly oriented transition dipole moments has a very limited light outcoupling efficiency since  $\hat{P}_a$  is widely scattered in randomly oriented nanocrystals.

### III. STRATEGIES FOR IMPROVING LUMINESCENCE EFFICIENCY

The intrinsic properties of MHPs such as long electron-hole diffusion length and small exciton binding energy at room temperature are well suited for their applications to solar cells but are not favorable for LED applications. This is because LED applications, in principle, require a high radiative recombination rate with a low defect density, effective exciton confinement, low optical loss, and charge balance in PeLEDs. To satisfy these requirements in 3D MHP films, optical properties and charge balance should be suitably modified during the deposition of MHP films and the fabrication of devices. In this section, we will present several recently reported findings and strategies for improving the LE of MHPs and PeLEDs. These strategies are based on the luminescence-limiting factors described previously and include (i) nanometer-scale control of particle dimension, (ii) dimensionality control to 2D and quasi-2D perovskites, (iii) ligand engineering of colloidal NCs and QDs, (iv) control of optical properties and charge balance, and (v) chemical modifications.

#### A. Nanometer-scale control of particle dimension

As discussed in Sec. II A, decreasing the physical dimension from micrometer scale to nanometer scale<sup>4,13</sup> and decreasing the dimensionality from 3D to 2D or 0D<sup>27</sup> are two most effective ways of increasing the LE of PeLEDs because these can enhance the LE of MHPs by confining the charge carriers and improving the possibility of radiative recombination of electron-hole pairs (excitons). It is now well known that the PL efficiency of perovskite emitters can be improved greatly if the exciton binding energy ( $E_b$ ) can be increased and the exciton diffusion length ( $L_D$ ) is decreased by reducing the grain size.<sup>5</sup> An ideal approach to achieve high  $E_b$  and low  $L_D$  in perovskite emitters is to effectively confine the excitons in

the form of nanometer-scale (<20 nm) colloidal perovskite nanoparticles (NPs) rather than in polycrystalline perovskite bulk films with large grain size (0.1–10  $\mu\text{m}$ ). These perovskite NPs are in totally different research subfields from polycrystalline perovskite bulk films. Perovskite NPs can be divided into two different regimes: (i) 0D perovskite quantum dots (QDs) with a dimension less than the exciton Bohr diameter,  $D_B$  (the quantum-size regime or strong quantum-confinement regime), and (ii) relatively less explored perovskite nanocrystals (NCs) with a dimension greater than  $D_B$  (the regime beyond the strong quantum confinement or beyond the quantum-size effect). Perovskite QDs with size less than  $D_B$  (<~10 nm) showed high  $E_b$  and low  $L_D$  and, thereby, achieved high PLQE at room temperature.<sup>1,73,90–93</sup> However, these 0D QDs suffer from strong dependence of emission wavelength and color purity on the QD size, as do inorganic QDs.<sup>94</sup>

The energy of confined excitons ( $E_{exc}$ ) in a spherical quantum well (i.e., 0D QD) with the radius  $R$  can be obtained by considering that  $E_{exc}$  is the sum of the following two distinct contributions: (i) the energy of strongly confined individual  $e$  and  $h$  particles [ $E(\alpha \rightarrow \infty)$ ] and (ii) the spatial  $e$ - $h$  correlation energy ( $E_{corr}$ ), where  $\alpha$  is a measure of the spatial  $e$ - $h$  correlation in an exciton with  $\alpha \rightarrow \infty$  for completely no correlation (individual particle confinement),<sup>95–97</sup>

$$E_{exc} = E(\alpha \rightarrow \infty) + E_{corr} \approx \frac{\hbar^2 \pi^2}{2\mu R^2} - \frac{C_1 e^2}{4\pi\epsilon_0\epsilon_r R} + E_{corr}(R \rightarrow 0) \\ = \frac{\hbar^2 \pi^2}{2\mu R^2} - \frac{C_1 e^2}{4\pi\epsilon_0\epsilon_r R} - 0.248E_b, \quad (15)$$

where  $\mu$  denotes the reduced mass of the exciton,  $E_{corr}(R \rightarrow 0)$  signifies the spatial  $e$ - $h$  correlation energy in the limit of  $R \rightarrow 0$ , and the binding energy  $E_b$  is defined in Eq. (1). In Eq. (15), the origin of energy ( $E_{exc}$ ) is chosen at the bandgap energy of the bulk crystal.<sup>98</sup> The first two terms in the last expression of Eq. (15) denote the kinetic energy of a very strongly confined individual particle ( $\hbar^2 \pi^2 / 2\mu R^2$ ) and the corresponding Coulomb energy ( $-C_1 e^2 / 4\pi\epsilon_0\epsilon_r R$ ) with the optimized  $C_1 = 1.786$ .<sup>95,96</sup> The asymptotic ground-state exciton wavefunction with a non-zero degree of the spatial  $e$ - $h$  correlation can be written, using the correlation parameter  $\alpha$ , as

$$\psi(r_e, r_h, r_{eh}) = N j_0\left(\frac{\pi r_e}{R}\right) j_0\left(\frac{\pi r_h}{R}\right) \exp\left(-\frac{r_{eh}}{\alpha}\right) \\ = N \frac{\sin(\pi r_e/R)}{r_e} \frac{\sin(\pi r_h/R)}{r_h} \exp\left(-\frac{r_{eh}}{\alpha}\right), \quad (16)$$

where  $N$  is the normalization constant,  $r_{eh}$  denotes the distance between the electron and hole in a given exciton quasi-particle ( $=|r_e - r_h|$ ), and  $j_0(x)$  designates the zeroth-order spherical Bessel function. Equation (16) shows that  $\psi(r_e, r_h, r_{eh})$  becomes a simple product of  $\psi(r_e)$  and  $\psi(r_h)$  for a strongly confined exciton under  $\alpha \rightarrow \infty$ . Under a strongly confined condition, the  $e$ - $h$  correlation in an exciton will be collapsed and  $E_{corr} \rightarrow 0$ . In this strongly confined limit ( $\alpha \rightarrow \infty$ ), the exciton Bohr radius [Eq. (1)] can be correlated with the critical QD radius for the PL blue shift ( $R_c$ ) using Eq. (15), namely,

$$\left(\frac{R_c}{a_B}\right) = \frac{4\pi\epsilon_0\epsilon_r \hbar^2 \pi^2}{2C_1 \mu e^2} = \frac{\pi^2}{2C_1} \approx 2.75. \quad (17)$$

We neglected the  $e$ - $h$  correlation energy ( $E_{corr} = -0.248E_b$ ) in the derivation of the above critical ratio. If we included the  $E_{corr}$  term

in  $E_{exc}$ , the resulting critical ratio ( $R_c/a_B$ ) would be significantly reduced. However, the exact degree of this reduction is not currently known and is an important task to complete.

Let us examine the effect of decreasing NC size on the PL properties (peak energy, linewidth, PLQE) and the critical size for the quantum-confinement effect using halide perovskite NCs. Kim *et al.*<sup>99</sup> recently demonstrated highly efficient LEDs based on the colloidal perovskite NCs in a dimension greater than the exciton Bohr diameter  $D_B$  (i.e.,  $2a_B$ ; the regime beyond the quantum-size effect). As shown in Figs. 4(a) and 4(b), the PL peak energy increases (blue shift in  $\lambda$ ) with decreasing dimension. This tendency becomes pronounced for the particle size smaller than  $\sim 10$  nm ( $D_B$ ). The PL spectrum of MAPbBr<sub>3</sub> NCs with size greater than 10 nm showed sharp peaks at  $\sim 515$  nm with the FWHM of  $\sim 23$  nm [Fig. 4(b)]. These perovskite NCs are beyond the quantum-size regime. The perovskite NCs with size  $\geq D_B$  (i.e., 11–27 nm) showed the highest PLQE ( $\sim 72\%$ ) among perovskite NPs [Fig. 4(c)]. The high PLQE of perovskite NCs is due to the increased  $E_b$  and the spatial exciton confinement in small NCs of the size close to  $D_B$ , which increases the electron–hole wavefunction overlap and radiative recombination rate by reducing the thermal ionization and delocalization of excitons.<sup>1,73,90,91</sup> In contrast, perovskite QDs with size less than  $D_B$  showed a gradually decreasing PLQE from  $\sim 65\%$  for 5 nm QDs to  $\sim 62\%$  for 3 nm QDs. This decrease can be attributed to the increase in trap-assisted recombination of excitons at surface traps due to the increased surface-to-volume ratio because the trap-assisted recombination is mainly related to the nonradiative recombination.<sup>69,73,100,101</sup>

According to the experimental results and theoretical arguments given in the previous paragraphs, the NC size should be sufficiently small for the enhanced  $E_b$  and the reduced  $L_D$ . However, it should be larger than  $D_B$  (i.e., beyond quantum-size effect) to

practically avoid a strong dependence of emission wavelength and color purity on the QD size and to minimize the trap-assisted nonradiative recombination at surfaces. The critical particle diameter [ $D_c$ ] deduced from these practical criteria is  $D_c/D_B \approx 1$ , where  $D_c$  can be viewed as the diameter for the onset of strong quantum confinement. For spherical NCs, this empirical rule now reads  $D_c/D_B = 2R_c/2a_B \approx 1$ . This ratio ( $\sim 1$ ) is much smaller than the critical ratio deduced from the PL blue shift [ $\sim 2.75$  in Eq. (17)]. However, if we alternatively adopt  $D_c$  of  $\sim 30$  nm for the onset of PL blue shift [Fig. 4(b)], then  $D_c/D_B \approx 30/10 \approx 3$ . This value qualitatively agrees with the theoretical ratio of 2.75 for the PL blue shift [Eq. (17)]. There still exists a small discrepancy between the theoretical and experimental values. As mentioned, the  $e$ - $h$  correlation energy, at least partly, contributes to this discrepancy.

In practice, the physical dimension or grain size of 3D MHPs can be reduced readily by nanocrystal pinning (NCP) in which dripping volatile solvents on the perovskite quasi-films during spin coating do wash out the remaining solvents [e.g., dimethyl sulfoxide (DMSO) and *N,N*-dimethylformamide (DMF)], quench the growth of perovskite crystals, and, thus, induce a reduced grain size [Fig. 5(a)].<sup>4,13,102</sup> NCP also effectively smoothens the surface morphology [Figs. 5(b) and 5(c)]. Grain size and film morphology can be controlled by suitably choosing the dripping solvents<sup>103,104</sup> and perovskite precursors.<sup>78</sup> The grain-size-reduction effect by NCP is maximized by adding organic semiconductors [e.g., TPBI; 2,2',2''-(1,3,5-benzinetriyl)-tris(1-phenyl-1-H-benzimidazole)], which can act as impurities that impede grain growth, into volatile solvents. In MAPbBr<sub>3</sub> films, a small grain size (average size of 87 nm) was achieved with TPBI [Fig. 5(d)].<sup>4,13</sup> The grain-boundary-filled TPBI also improves the charge balance and the electron injection efficiency in MAPbBr<sub>3</sub> emitting layers and heals the defect states on the

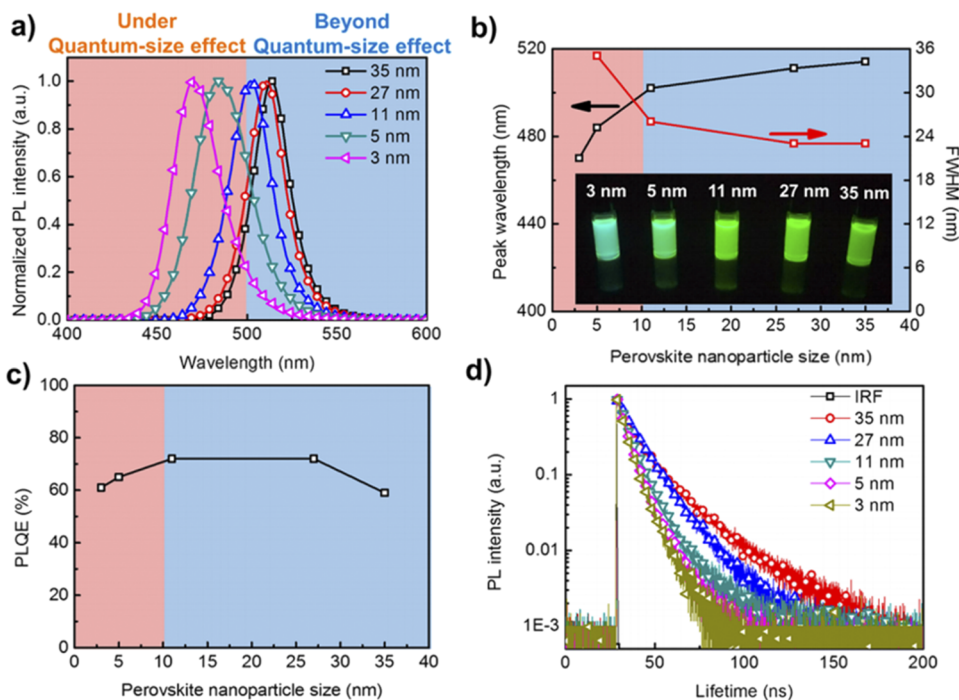


**FIG. 4.** (a) PL spectra of perovskite NPs, (b) maximum PL peak wavelengths and FWHM of perovskite NPs and photograph of perovskite NPs under a  $\lambda = 350$  nm Xe lamp (inset), (c) PLQE of the perovskite NPs under 400 nm excitation, and (d) PL lifetime curves of perovskite NPs obtained from TCSPC (time-correlated single-photon counting). The kinetic measurements were carried out to understand the size effect on the dynamics of excitons in perovskite NPs. All the samples showed a much shorter average lifetime ( $\tau_{av}$ ) than bulk perovskite films ( $\sim 100$  ns).<sup>4</sup> The reduced lifetime indicates that the rapid PL decay of perovskite NPs is mainly caused by the geminate electron–hole recombination, owing to enhanced  $E_b$  and electron–hole overlap, rather than by free-carrier recombination. Reproduced with permission from Kim *et al.* ACS Nano 11, 6586 (2017). Copyright 2017 American Chemical Society.

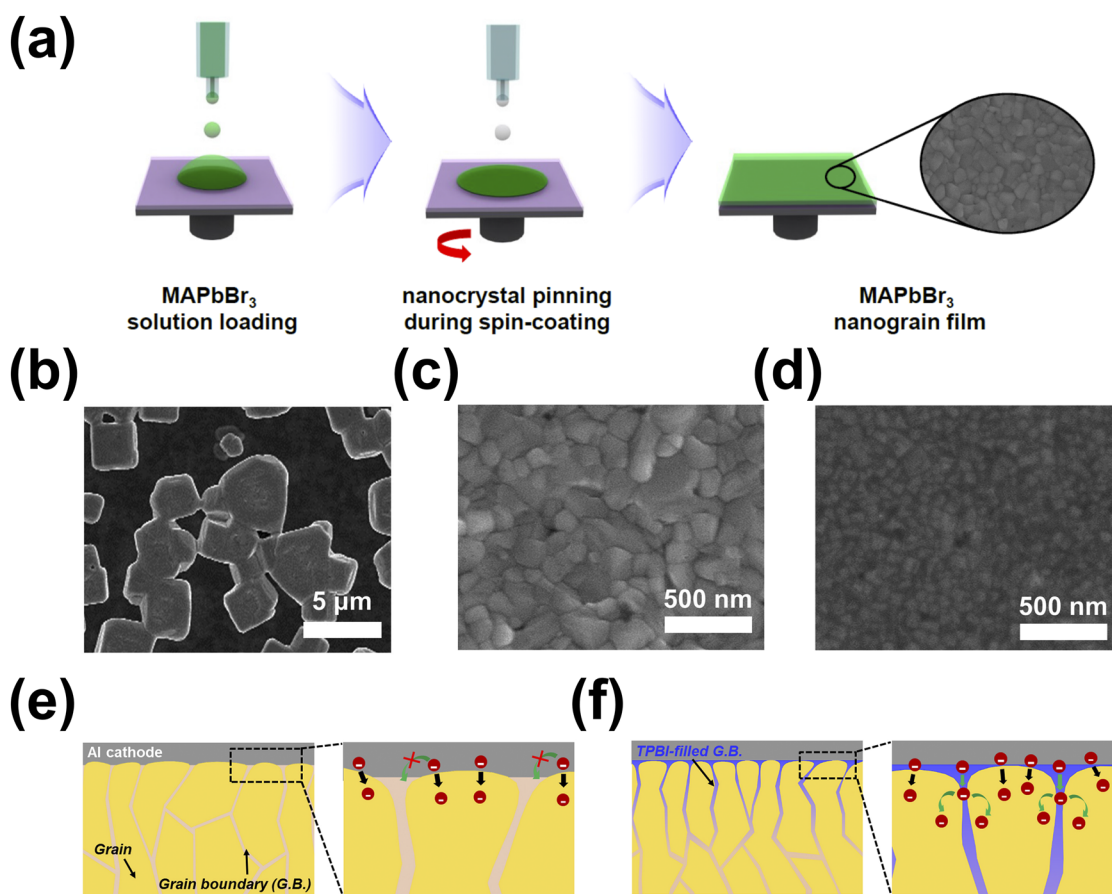


**FIG. 5.** Several illustrations related to the nanocrystal pinning (NCP). (a) Schematic illustration describing the NCP process. [(b)–(d)] Scanning electron-microscope images of MAPbBr<sub>3</sub> polycrystalline films (b) without NCP, (c) with NCP, and (d) with TPBi based NCP. Reproduced with permission from Cho *et al.* *Science* **350**, 1222 (2015). Copyright 2015 The American Association for the Advancement of Science. [(e) and (f)] Schematic illustrations of the trap-filling and electron-injection improvement effect by additive-based NCP (A-NCP). Reproduced with permission from Park *et al.* *Nano Energy* **42**, 157 (2017). Copyright 2017 Elsevier Ltd.

grain boundaries [Figs. 5(e) and 5(f)], yielding PeLEDs with high EQEs (~8.79%).<sup>13</sup>

## B. Dimensionality control to 2D and Quasi-2D perovskites

The dimensionality control from 3D to 2D is one of the most effective ways of increasing the LE of PeLEDs, as mentioned in Sec. III A. 2D MHPs, in which a PbX<sub>6</sub> octahedral layer is sandwiched between large or long organic ammonium (OA) layers, showed more strongly confined electron–hole pairs in PbX<sub>6</sub> inorganic layers and much lower trap density than 3D MHPs (MAPbI<sub>3</sub>). These cause  $k_1$  to be related to  $k_{1(exc)}$  rather than to  $k_{1(def)}$  [Eq. (3)] and increase PLQE.<sup>37,105</sup> However, in 2D MHP polycrystalline bulk films and PeLEDs based on them, bulky insulating OA groups inhibit charge transport and, thereby, limit EL efficiency in PeLEDs.<sup>27</sup> To achieve moderate charge-transport characteristics while maintaining efficient confinement of electron–hole pairs, quasi-2D structures, called Ruddlesden–Popper (RP) phase, were incorporated by mixing 3D

perovskites with 2D perovskites. The average number of layers of PbX<sub>6</sub> octahedral planes [dimensionality, i.e.,  $n$  in (OA)<sub>2</sub>(MA or FA)<sub>*n*-1</sub>Pb<sub>*n*</sub>X<sub>3*n*-1</sub>;  $n$  = from 1 (2D structure) to ∞ (3D structure)] can be tailored by controlling the mixing ratio between 2D perovskite precursors and 3D perovskite precursors.<sup>27</sup> The large OA cations intercalate between separated 3D perovskites by relatively weak van der Waals interactions.<sup>37</sup>

In this way, they confine the electron–hole pairs inside the 3D perovskites and, thereby, prevent the dissociation of electron–hole pairs into free-charge carriers. As a result, radiative recombination of electron–hole pairs is enhanced. This enhanced effect was confirmed by observing a much shorter PL lifetime of quasi-2D MHPs (~20 ns) than that of 3D MHPs (~1200 ns) and a linear dependence of the PL intensity on the injected carrier density.<sup>37</sup> Quasi-2D MHPs also showed higher  $E_b$  (>200 meV for (PEA)<sub>2</sub>(MA)<sub>*n*-1</sub>Pb<sub>*n*</sub>I<sub>3*n*-1</sub>) than 3D MHPs (~20 meV for MAPbI<sub>3</sub>).<sup>43</sup> However, in 2D and quasi-2D MHP polycrystalline bulk films, a strong exciton–LO phonon coupling, which is caused by many dangling bonds (e.g., out-of-plane self-terminations of PbX<sub>6</sub> octahedra) and excess excitons due to

efficient spatial confinement, can also limit the LE, as described in Sec. II C.<sup>37</sup> Therefore, optimum MHP crystal structures having efficient exciton confinement, moderate charge transport, and low exciton–LO phonon coupling should be developed to maximize the LE in PeLEDs.

Quasi-2D MHPs are composed of various perovskite structures having different dimensionalities. This kind of structural arrangement induces energy transfer from a quasi-2D region with a larger bandgap (small  $n$ ) to a neighboring 2D region with a smaller bandgap (large  $n$ ).<sup>5</sup> This energy transfer induces a higher concentration of the electron–hole pairs (excitons) in the crystalline regions of relatively smaller bandgaps and, consequently, achieves a high PLQE under a low excitation density.<sup>43</sup> Thus, when quasi-2D MHPs have large-bandgap crystals as major components with a relatively graded dimensionality distribution, the energy transfer will be boosted; thus, the PLQE can be enhanced.

Quasi-2D MHP films also showed a reduced trap density and a reduced number of nonradiative recombination channels, as compared with the 3D MHP films because large OA can passivate the surface defects in 3D MHP films.<sup>106</sup> This effect was confirmed by measuring the trap density of states in PeLEDs<sup>27</sup> and by observing a pronounced increase in the PLQE [from 1%–2% for MAPbBr<sub>3</sub> to 34% for (PEA)<sub>2</sub>(MA) <sub>$n-1$</sub> Pb <sub>$n$</sub> Br <sub>$3n-1$</sub> <sup>27</sup> and from 0.2% for MAPbI<sub>3</sub> to 10.6% for (PEA)<sub>2</sub>(MA) <sub>$n-1$</sub> Pb <sub>$n$</sub> I <sub>$3n-1$</sub> <sup>43</sup>]. Quasi-2D MHPs also showed much faster recombination rates ( $k_1 \approx 5 \times 10^7 \text{ s}^{-1}$ ,  $k_2 \approx 2 \times 10^{-9} \text{ cm}^3 \text{ s}^{-1}$ , and  $k_3 \approx 2 \times 10^{-26} \text{ cm}^6 \text{ s}^{-1}$ ) than 3D MHPs ( $k_1 \approx 9 \times 10^5 \text{ s}^{-1}$ ,  $k_2 \approx 7 \times 10^{-10} \text{ cm}^3 \text{ s}^{-1}$ , and  $k_3 \approx 3 \times 10^{-28} \text{ cm}^6 \text{ s}^{-1}$ ).<sup>37</sup> These indicate that quasi-2D MHPs have much higher PLQEs in LED operating conditions (charge carrier density of  $<10^{15} \text{ cm}^{-3}$ ) than 3D MHPs.

### C. Ligand engineering of colloidal NCs and QDs

Although colloidal MHP NCs and QDs have high PLQE in solution states, the first reported PeLEDs based on MHP QDs showed very low EL efficiencies: EQE  $\approx 0.07\%$ , CE  $\approx 0.14 \text{ cd A}^{-1}$ , and power efficiency (PE)  $\approx 0.07 \text{ lm W}^{-1}$  for blue emission; EQE  $\approx 0.12\%$ , CE  $\approx 0.43 \text{ cd A}^{-1}$ , and PE  $\approx 0.18 \text{ lm W}^{-1}$  for green emission; and EQE  $\approx 0.09\%$ , CE  $\approx 0.08 \text{ cd A}^{-1}$ , and PE  $\approx 0.06 \text{ lm W}^{-1}$  for orange emission.<sup>107</sup> This discrepancy can mainly be attributed to the following two observations: (i) NCs and QDs tend to agglomerate in highly concentrated solutions ( $>0.5 \text{ mg mL}^{-1}$ )<sup>108</sup> or fabrication of uniform and thick NC and QD films is very difficult in film processing steps<sup>99</sup> and (ii) insulating organic ligands (e.g., oleylamine, oleic acid), which are necessary to stabilize NCs and QDs in solutions, severely impede charge injection and transport in NC films.<sup>99,109</sup> Reduced PLQE of MHP NCs and QDs, especially CsPbBr<sub>3</sub> QDs, when they constitute a film, further limits the EL efficiency.

Many research groups have tried various strategies to fabricate uniform and thick NC films and to obtain highly efficient PeLEDs based on them. The surface coverage can be improved by mixing NCs with poly(methylmethacrylate) (PMMA).<sup>110</sup> The PMMA matrix having a low dielectric permittivity increases  $E_b$  ( $\sim 161.6 \text{ meV}$ ) and PLQE ( $\sim 92\%$ ) of NC films by inducing the dielectric confinement effect and, thereby, achieves a high EL efficiency (EQE  $\approx 3.04\%$  and CE  $\approx 13.02 \text{ cd A}^{-1}$ ) in PeLEDs.<sup>110</sup> TMA (trimethylaluminum) treatments also dramatically increased PLQE of NC films from  $\sim 25\%$  to  $\sim 85\%$  by passivating the surface defects and achieved high EL efficiencies in PeLEDs (EQE  $\approx 5.7\%$  in red

emission).<sup>111</sup> Cross-linking the organic ligands by using initiators or heat treatment is also an effective method. For example, MHP NCs capped with 4-vinylbenzyl dimethyl-octadecylammonium chloride can readily be cross-linked by an initiator (azobisisobutyronitrile), and the resulting cross-linked NC films are characterized by homogeneous film morphology and show a high PLQE ( $\sim 56\%$ ).<sup>112</sup> Cross-linking by x-ray irradiation<sup>113</sup> can also increase the density of NC films and facilitate the charge transport.

Even though uniform MHP NC and QD films are fabricated and high PLQE is achieved in NC and QD films, their EL efficiencies in green PeLEDs have not been still higher than those of MHP bulk films for a recent few years: CsPbBr<sub>3</sub>/MABr quasi-core/shell structure recently showed a record high EQE of 20.3%.<sup>16</sup> That is because insulating organic ligands hinder efficient charge injection or transport from the electrodes or within the NC and QD films. Post-ligand engineering is an effective method to reduce the ligand length and density.<sup>114,115</sup> Replacing long ligands [oleic acid (RCOOH) and oleylamine (RNH<sub>2</sub>)] with di-dodecyl dimethyl ammonium bromide greatly improves the charge transport characteristics and increases EQE from  $\sim 0.1\%$  to  $\sim 3\%$  in PeLEDs [Fig. 6(a)].<sup>114</sup> Washing synthesized QDs with hexane/ethyl acetate cosolvents in which ethyl acetate is a solvent with moderate polarity ( $\sim 4.3$ ) can effectively reduce the surface ligand density [Fig. 6(b)]. Washing  $\leq 3$  times can effectively reduce the surface ligand density, improve the charge transport characteristics while maintaining high PLQE of QDs, and achieve high EL efficiencies in PeLEDs (EQE  $\sim 6.27\%$  and CE  $\sim 13.3 \text{ cd A}^{-1}$ ).<sup>116</sup> Conducting both ligand-exchange and washing process is more effective to improve the EL efficiencies (EQE  $\approx 6.25\%$ , CE  $\approx 18.8 \text{ cd A}^{-1}$ , and PE  $\approx 18.9 \text{ lm W}^{-1}$ )<sup>117</sup> than doing either process individually.

*In situ* methods can be used to control ligand length and density on the surface of MHP NCs [Figs. 6(c) and 6(d)].<sup>99,109</sup> When NCs were synthesized using recrystallization methods, reduction in the density<sup>99</sup> or length<sup>109</sup> of ligands caused an increase in the NC size in the regime beyond the quantum size effect. In these NCs, luminescent quenching at the surface defects was suppressed, so the NCs showed size-independent high color purity and PLQE. Furthermore, these NC films had reduced length and density of ligands and, therefore, showed enhanced charge transport characteristics. With these methods, highly efficient PeLEDs based on MAPbBr<sub>3</sub> NCs (EQE  $\approx 5.09\%$  and CE  $\approx 15.5 \text{ cd A}^{-1}$ )<sup>99</sup> and FAPbBr<sub>3</sub> NCs (EQE  $\approx 2.05\%$  and CE  $\approx 9.16 \text{ cd A}^{-1}$ )<sup>109</sup> were achieved. More recently, CsPbBr<sub>3</sub> red QDs with the EQE of 21.3% were successfully fabricated by adopting the anion-exchange method.<sup>117</sup>

### D. Control of optical properties and charge balance

As described previously, LED applications require a high radiative recombination rate with a low defect density, effective exciton confinement, low optical loss, and charge balance in PeLEDs. To satisfy these requirements in 3D MHP films, optical properties and charge balance should be suitably modified during deposition of the MHP film and fabrication of the devices. Multilayer PeLEDs are composed of MHP emitting layers, organic charge transport layers, and electrodes. Optical energy loss in planar LEDs is a result of the surface plasmon, waveguide mode, and substrate mode. In particular, the refractive index  $n_r$  is generally higher in solution-processed MHP films ( $n_r = 2.2\text{--}2.6$ ) than in organic films

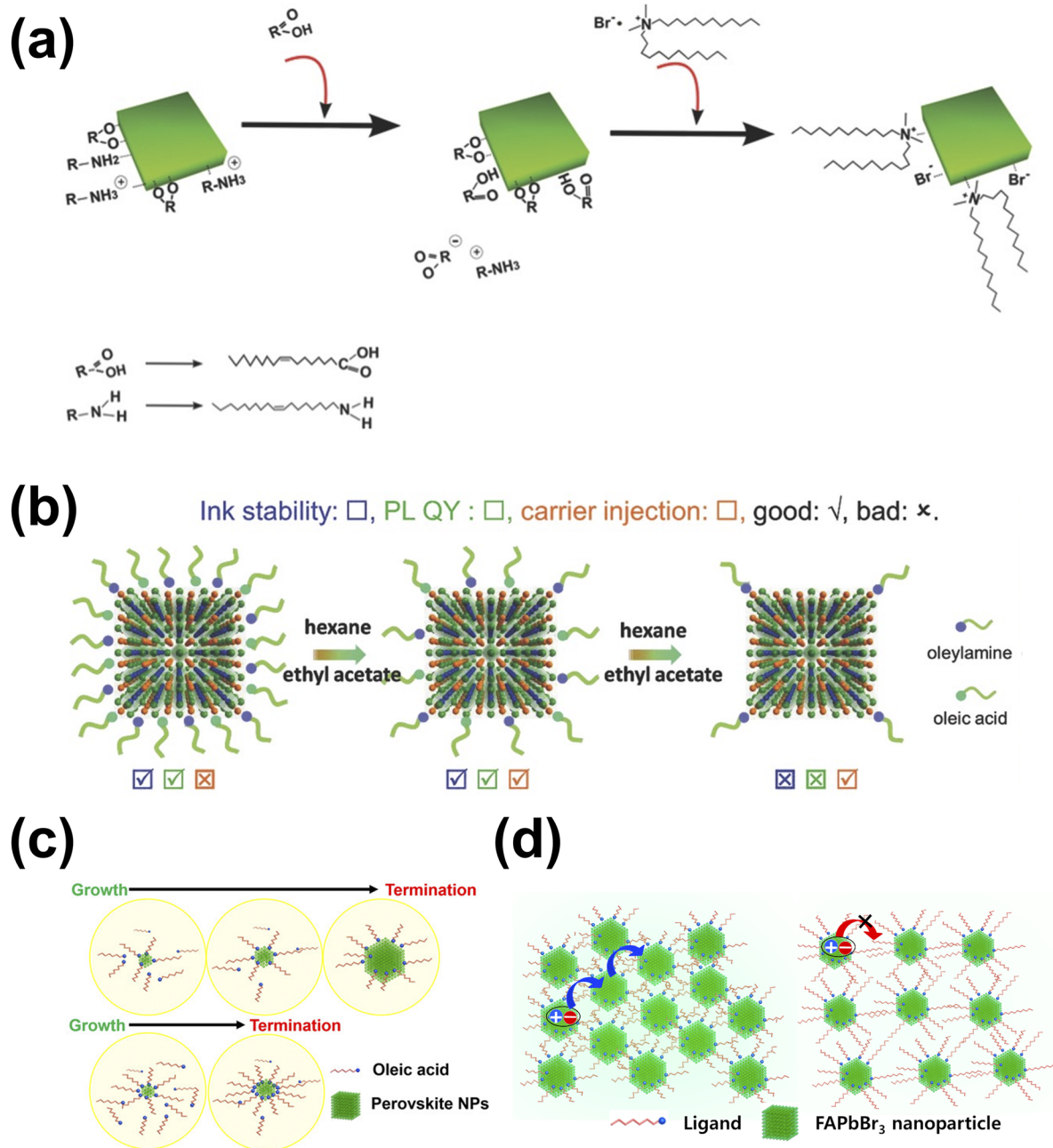


**FIG. 6.** Schematic illustrations of ligand engineering for colloidal nanocrystals (NCs). (a) Schematic illustration describing the post-ligand exchange. Reproduced with permission from Pan *et al.* *Adv. Mater.* **28**, 8718 (2016). Copyright 2016 Wiley-VCH. (b) Schematic illustration of the post-ligand density control by purification. Reproduced with permission from Li *et al.* *Adv. Mater.* **29**, 1603885 (2017). Copyright 2017 Wiley-VCH. (c) Schematic illustration describing the *in situ* control of ligand density during NC synthesis. Reproduced with permission from Kim *et al.* *ACS Nano* **11**, 6586 (2017). Copyright 2017 American Chemical Society. (d) Schematic illustration of charge transport in NC films with different ligand lengths (left: short; right: long). Reproduced with permission from Kim *et al.* *Nano Energy* **38**, 51 (2017). Copyright 2017 Elsevier Ltd.

( $n_r = 1.4\text{--}2.0$ ), so  $n_r$  varies greatly across the interface between them. As a result, the waveguide mode of the total reflection of emitting light at the interface of MHP emitting layers can be a major optical energy loss in PeLEDs.<sup>118,119</sup> Therefore, modifying the optical

properties is a simple but very effective approach to improving the light outcoupling of PeLEDs. Optical simulation under the assumptions of ideal charge balance, PLQE, and film conditions (i.e., without considering defects and surface morphology condition)

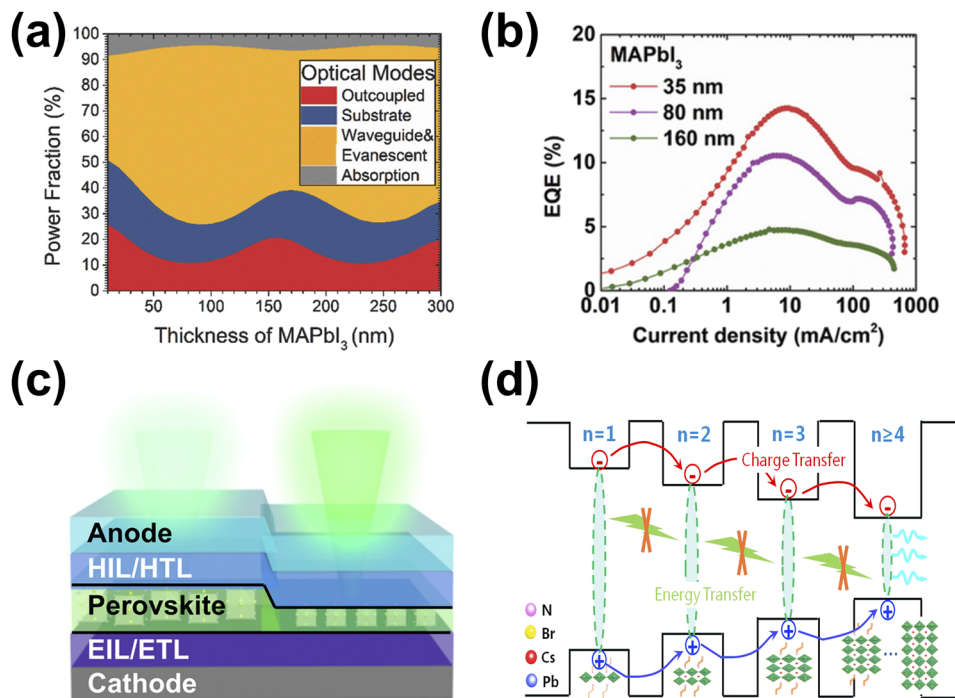


**FIG. 7.** Data and illustrations related to optical engineering of MHP-based PeLEDs. (a) 3D MAPbI<sub>3</sub> ( $n_r = 2.6$ ) PeLED depending on the thickness of the MHP emitting layer. Adapted with permission from Shi *et al.* *Adv. Opt. Mater.* **6**, 1800667 (2018). Copyright 2018 Wiley Online Library. (b) EQEs of PeLEDs depending on the MAPbI<sub>3</sub> thickness. Adapted with permission from Zhao *et al.* *Adv. Mater.* **31**, 1805836 (2019). Copyright 2019 Wiley Online Library. (c) Schematic illustration of optical outcoupling in polycrystalline PeLEDs depending on the thickness of the emitting layer. (d) Schematic images of energy and charge carrier cascade in multi-quantum wells of quasi-2D MHPs. Adapted with permission from Chen *et al.* *Nano Energy* **50**, 615 (2018). Copyright 2018 Elsevier Ltd.

suggested that the light interference effect can be induced by the high  $n_r$  of 3D MHP films. Thus, the outcoupling effect can be improved by sensitively controlling the thickness of 3D MHP emitting layers [Fig. 7(a)].<sup>120</sup> As shown in Fig. 7(b), the waveguide optical loss was significantly reduced to effectively improve the light outcoupling and EQEs from 4.8% (160 nm thickness) to 14.3% (35 nm thickness) of the MAPbI<sub>3</sub> PeLEDs.<sup>119</sup>

Reducing the  $n_r$  value of MHP films can also be effective to minimize the waveguide mode optical loss in PeLEDs [Fig. 7(c)].<sup>121</sup> The  $n_r$  value is influenced by the density of a dielectric medium ( $d_p$ ) with the porosity  $\rho$ . Using the Lorentz–Lorenz relationship, one can establish the following expression for the density-dependent  $n_r$  for a dielectric medium:

$$n_r = \left[ \frac{1 + 2P_m}{1 - P_m} \right]^{1/2}. \quad (18)$$

In the above equation,  $P_m$  is defined as  $P_m \equiv (4\pi/3)N\alpha_m$  in centimeter-gram-second units, where  $N$  is the number of constituting molecules per unit volume of a nonporous crystalline medium and  $\alpha_m$  denotes the mean polarizability. For a porous medium, it is not difficult to replace  $N$  with  $(d_p N_o)/(M_w(1 - \rho))$ , where  $N_o$  is the Avogadro number and  $M_w$  is the molar mass (molecular weight) of constituting molecules. Thus,  $P_m$  for a porous dielectric medium can be written as  $P_m = (4\pi N_o \alpha_m d_p)/(3M_w(1 - \rho))$ , where  $d_p/(1 - \rho) = NM_w/N_o$  is a fixed material quantity which is independent of  $\rho$ . According to Eq. (11),  $n_r$  increases with increasing  $P_m$  (i.e., with increasing  $d_p$  or with decreasing  $\rho$ ). Thus, a low  $n_r$  value can be obtained from the porous MHP layer having a low density.<sup>122,123</sup> The light emitted from the MHP layers passes through complex media, including grains and grain boundary regions that are formed during the crystallization process. The  $n_r$  value is significantly affected by

the deposition method and, consequently, by crystallinity:  $n_r = 2.5$  for a single-crystalline MHP film,  $n_r = 2.2$  for a solution-processed MHP film, and  $n_r = 1.8$  for a vacuum-processed MHP film.<sup>124</sup> Thus, the decrease in  $n_r$  can be correlated with the decrease in density or with the increase in the porosity of the MHP film. Optical simulation showed that the outcoupling efficiency is remarkably improved from 7% to 25% (i.e., 350% increase) as the  $n_r$  value is reduced from 2.5 to 1.6 (i.e., 36% decrease).<sup>124</sup> Therefore, controlling optical properties of MHP films (by adjusting  $n_r$  and thickness) and optimally designing the device architecture are highly effective approaches to achieve optimal EQEs in PeLEDs.

EL efficiency in LEDs is effectively determined by the charge balance, recombination rate of electron–hole pairs, and PLQE of the emitting film in devices. Compared to 3D polycrystalline MHPs, low-dimensional (2D or 0D) MHPs have higher exciton binding energies and effective exciton confinements due to the quantum-confinement effects in nanoscale domains surrounded by bulky insulating organic cations or organic ligands.<sup>43,125–127</sup> In 2D MHPs, a few PbX<sub>6</sub> (X = Cl, Br, I) layers are sandwiched by adding bulky organic cations such as phenylethylammonium (PEA) or butylammonium (BA) to achieve a multi-quantum well structure that yields a large exciton binding energy and strong exciton confinement.<sup>27</sup> In 0D MHPs, PbX<sub>6</sub> octahedra that are isolated by insulating ligands effectively confine excitons, resulting in a high exciton binding energy.<sup>99</sup> Furthermore, CsPbX<sub>3</sub> (X = halides) quantum dots (QDs) have achieved PLQE higher than 90%.<sup>128</sup> The low dimensionalities of 2D and 0D MHPs are theoretically beneficial to achieving high external PLQEs of the films, which leads to high EL efficiencies. However, the external PLQE of the MHP films can be reduced by photon recycling and low outcoupling efficiency that arise from the high  $n_r$  of MHPs.<sup>40,97</sup> Thus, passivation of surface defects in

3D polycrystalline MAPbI<sub>3</sub> film has given a high internal PLQE = 91.9% at the photon flux of 60 mW/cm<sup>2</sup> at 532 nm, although an external PLQE showed 37%.<sup>40,118</sup> This high internal PLQE of 3D MHPs suggests that 3D polycrystalline MHP films possibly have a high radiative recombination rate, but high external PLQE may be degraded by bulk and surface defects and by high  $n_r$ . Therefore, an ideal EQE of up to 25%–30% in 3D polycrystalline PeLEDs can be achieved when the low external PLQE is overcome by defect passivation and effective light outcoupling.

Although the grain boundary has been reported as a charge-transporting barrier, charge separator, and charge trapping site in 3D MHPs,<sup>10,129</sup> the charge-transporting property is more beneficial in 3D MHPs than in 2D and 0D PeLEDs having bulky organic cations or insulating ligands.<sup>130</sup> Furthermore, the contribution of the charge transfer is more important than the energy transfer for the EL efficiency of quasi-2D PA<sub>2</sub>(CsPbBr<sub>3</sub>)<sub>y-1</sub>PbBr<sub>4</sub> PeLEDs that are accompanied by efficient energy confinement during electrical device operation [Fig. 7(d)], where PA is the propylammonium group and “y” denotes the number of PbBr<sub>6</sub> layers between bulky organic layers.<sup>18</sup> In particular, the charge balance and confinement depending on charge-carrier cascades from high to low bandgap states (i.e., MHP units with large y) in quasi-2D MHP films are not efficient because of the energy level differences between multi-quantum well MHP units and the imbalanced electron and hole cascade.<sup>18</sup> Charges can accumulate and device efficiency is reduced significantly at high driving voltages. Therefore, the charge-transporting property is an important parameter in the luminescent properties of PeLEDs. The electrical transport property can be improved when 3D MHPs are used, instead of low-dimensional MHPs, and the efficiency of PeLEDs can be effectively improved when the defective grain boundary region becomes benign.

A kinetically controlled organic-shielded nanograin (OSN) film mimicking core-shell nanoparticles was recently developed using MAPbBr<sub>3</sub> as a core and organic semiconducting additive TPBI as a shell (MAPbBr<sub>3</sub>:TPBI).<sup>84</sup> Small perovskite nanograin cores shielded with a uniform TPBI additive provide efficient defect passivation and exciton confinement within a nanograin. This OSN promotes

a high radiative recombination rate throughout the film and facilitates effective light outcoupling owing to decreased refractive index of the OSN emitting layer. As a result, the MAPbBr<sub>3</sub>:TPBI (OSN) PeLED achieved high device efficiencies [EQE = 21.81% ph e<sup>-1</sup>; CE = 87.35 cd A<sup>-1</sup> with a half-sphere (HS) lens; Fig. 8]. Moreover, the device half-lifetime of MAPbBr<sub>3</sub>:TPBI (OSN) PeLED was highly improved more than four-times than MAPbBr<sub>3</sub> (A-NCP) PeLED [ $t_{50}$  = 251 min for MAPbBr<sub>3</sub>:TPBI (OSN) vs 58.2 min for MAPbBr<sub>3</sub> (A-NCP)] because of more uniform electron-hole recombination and reduced ion migration throughout the film with uniform TPBI distribution.<sup>84</sup>

It has been shown that the introduction of oriented emitters has remarkably increased the EQE of OLEDs to almost 40%.<sup>131,132</sup> Randomly oriented transition dipole moments have limited the light outcoupling efficiency of all isotropic light sources, including perovskites. As suggested in Sec. II E, anisotropic materials with oriented transition dipole moments will be desirable to further improve the luminescence efficiency of the films and devices. Recent first-principles calculations by Rivett and co-workers<sup>133</sup> found intrinsic anisotropies in the transition dipole moment in MAPbI<sub>3</sub> perovskites, which depend on the orientation of light polarization and the polar distortion of the local crystal lattice. Jurow *et al.*<sup>134</sup> have synthesized colloiddally stable CsPbBr<sub>3</sub> perovskite nanoplates and used them as quantum-confined blue light emitters with orientable transition dipole moments. By reducing the dimensions of the nanocrystals and depositing them face down onto a substrate by spin coating, they were able to orient the average transition dipole moment of films into the plane of the substrate and improve the emission properties for light emitting devices.<sup>134</sup> They then exploited the sensitivity of the perovskite electronic transitions to the dielectric environment at the interface between the crystal and their surroundings to reduce the angle between the average transition dipole moment and the surface to only 14° and maximize potential light emission efficiency.<sup>134</sup> This tunability of the electronic transition that governs light emission in perovskites is unique and introduces a valuable method to further extend the efficiencies and applications of perovskite-based photonic devices.

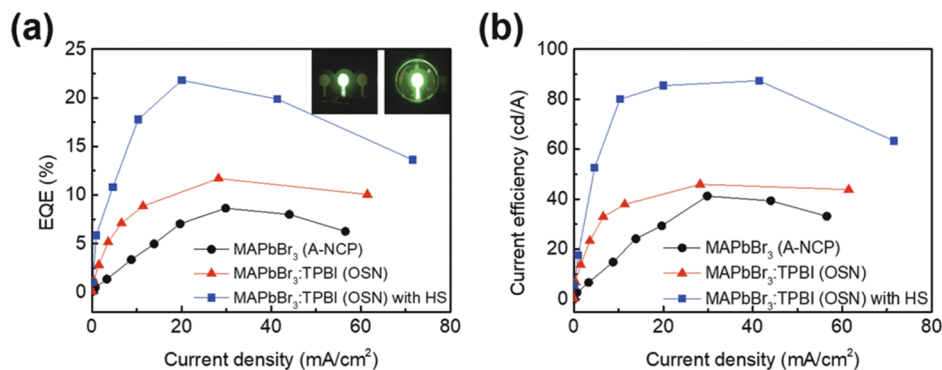


**FIG. 8.** Device characteristics of PeLEDs based on (i) MAPbBr<sub>3</sub> (A-NCP), (ii) MAPbBr<sub>3</sub>:TPBI (OSN) emitting layers, and (iii) OSN PeLED with half-sphere lens (HS), where A-NCP signifies the additive-based NCP in which instantaneous nucleation and a rapid crystal growth occur by drastically changing the solubility state of the spinning halide perovskites [Fig. 5(a)]. (a) EQE vs current density (inset: emitting pixels without and with HS). (b) Current efficiency vs current density. Reproduced with permission from Park *et al.* Adv. Funct. Mater. **29**, 1902017 (2019). Copyright 2019 Wiley-VCH.

## E. Chemical modifications

One challenging aspect of polycrystalline MHP thin films is that they inevitably form high density defect states. Moreover, MHP crystals tend to have polar and soft ionic lattices with lattice tilting and distortion, which results in atomic vacancies and high chemical reactivity, so they are vulnerable.<sup>135</sup> Therefore, the MHP structure has various ionic trap states as well as defect chemical states.<sup>47</sup> Charge carriers can readily be trapped or quenched by trap states such as metallic interstitial defects or halide vacancies. As a result, EL efficiency can be reduced drastically.<sup>136</sup> One efficient strategy to overcome this problem is the removal of metallic quenching sites such as metallic Pb atoms in the perovskite structure.<sup>4,137</sup> Metallic atoms that remain after a certain incomplete reaction between precursors can act as a strong quencher for excitons by dipole-dipole interaction, which facilitates nonradiative recombination loss.<sup>4,138</sup> Stoichiometry engineering employing excess organic cations has been used to remove metallic Pb atoms and reduce exciton quenching [Fig. 9(a)].<sup>4,137,139</sup> PL lifetimes extracted from transient PL data have shown that uncoordinated metallic Pb atoms cause strong nonradiative recombination. PL lifetime can be prolonged by removing the metallic Pb atoms, and the increase in the device efficiency can be ascribed to the reduction in exciton quenching by fine stoichiometric control [Figs. 9(b) and 9(c)].

Compositional engineering can be used to enhance the intrinsic chemical stability and to suppress the electronic trap states in

the perovskite lattice. Substitution of widely used MA cations with other cations, including FA<sup>+</sup>, Cs<sup>+</sup>, rubidium (Rb<sup>+</sup>), K<sup>+</sup>, or a mixture of these, has shown to be effective for enhancing the structural stability and photophysical properties.<sup>140,141</sup> In particular, the systematic analysis on structural and optical properties of FA<sub>x</sub>Cs<sub>1-x</sub>PbBr<sub>3</sub> or FA<sub>x</sub>Rb<sub>1-x</sub>PbBr<sub>3</sub> revealed that incorporating a small amount of alkali cations into perovskite lattices effectively stabilizes the chemical state of Pb<sup>2+</sup> ions and PbBr<sub>6</sub> octahedra, resulting in a low trap density and enhanced EL efficiency with suppressed photoinduced and electrically driven degradation.<sup>15,142</sup> Moreover, the Pb substitution with other divalent metals such as Cd or Zn reported in solar cell applications has indicated a possibility of further structural stabilization and enhancement of photophysical properties of 3D MHPs.<sup>143</sup>

Chemically passivating defect states at the grain boundaries are also important because nanograin engineering inevitably causes a high density of grain boundary regions.<sup>144</sup> Uncoordinated ions occur at the grain surface, mostly as a result of the formation of ionic defects with a low formation energy such as halogen or MA vacancies and interstitials.<sup>145</sup> These defects remain as charged defects, trap charge carriers, or dissociate the excitons into free charges.<sup>146</sup>

Theoretical studies and direct observation by confocal PL microscopy have shown that chemical treatment of nonstoichiometric grain surfaces with uncoordinated Pb atoms can strongly affect the PL efficiency of MHP films.<sup>68</sup> Electron-rich molecules can passivate undercoordinated Pb<sup>2+</sup> ions in MHPs and, thereby,

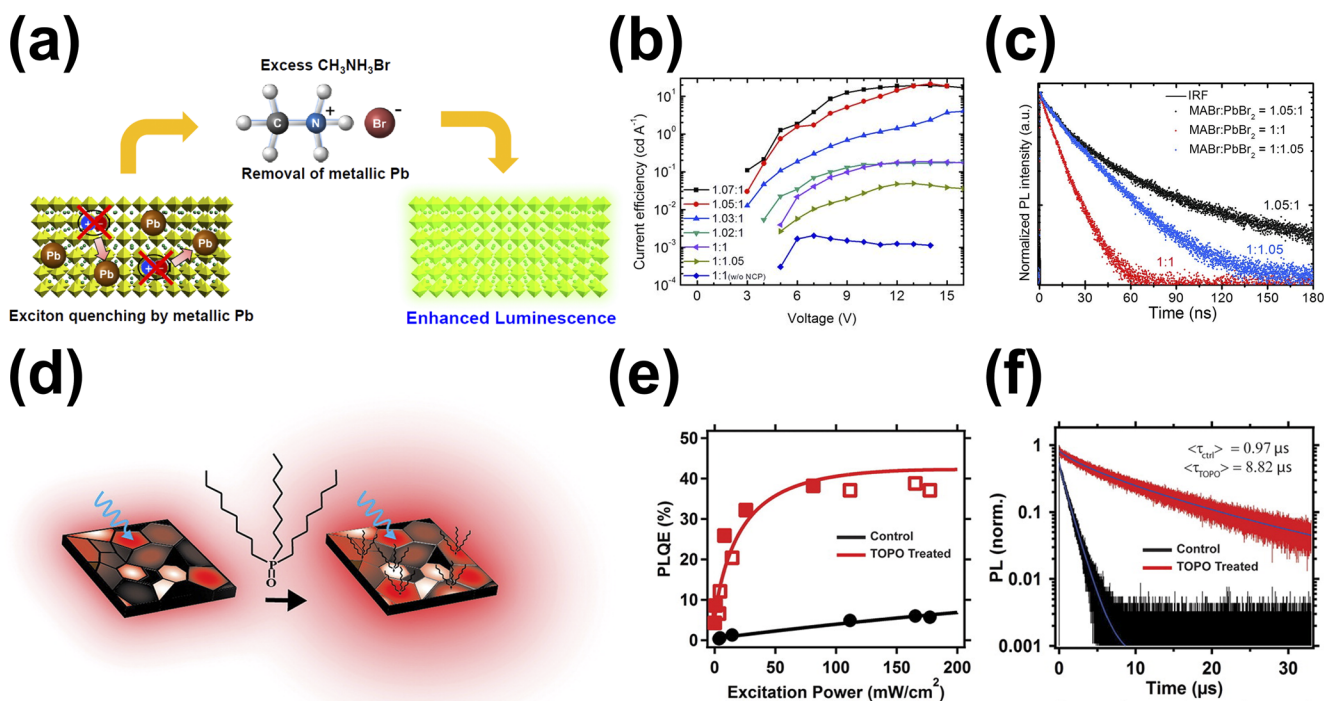


**FIG. 9.** (a) Schematic illustration of stoichiometry control using excess MABr to prevent exciton quenching from metallic Pb atoms. (b) Current efficiency and (c) PL lifetime of perovskite thin films based on NCP and MAPbBr<sub>3</sub> nanograin emission layers with varying molar ratio of MABr:PbBr<sub>2</sub>. Adapted with permission from Cho *et al.* *Science* **350**, 1222 (2015). Copyright 2015 The American Association for the Advancement of Science. (d) Schematic illustration of post-ligand treatment using tri-*n*-octylphosphine oxide (TOPO). (e) Photoluminescence quantum efficiency (PLQE) and (f) PL lifetime of control (black) and TOPO-treated films (red). Adapted with permission from Noel *et al.* *ACS Nano* **8**, 9815 (2014). Copyright 2016 American Chemical Society.

suppress charge trapping and nonradiative recombination. Moreover, surface treatment of MHP films with electron-rich Lewis base molecules such as pyridine, thiophene, and tri-*n*-octylphosphine oxide (TOPO) has dramatically increased the PL lifetimes and PLQEs by neutralizing and deactivating positively charged defects [Figs. 9(d)–9(f)].<sup>147,148</sup> Lewis-basic PEG-doped CsPbBr<sub>3</sub> for PeLEDs has been achieved by inducing a dative bonding between electron-rich oxygen atoms and uncoordinated Pb<sup>2+</sup> defects.<sup>149</sup> The maximum PLQE was much higher (35%) in the PEG-doped CsPbBr<sub>3</sub> film than in the pristine CsPbBr<sub>3</sub> film, and the optimized PeLEDs achieved CE<sub>max</sub> of 19 cd/A and EQE<sub>max</sub> of 5.34%.<sup>148</sup> Further in-depth investigations are needed to achieve high internal quantum efficiency without nonradiative losses from chemically defect states.

#### IV. DIRECTIONS FOR FUTURE RESEARCH

The research of MHP-based PeLEDs can be classified into three subareas according to the dimensionality of involving perovskites: (i) 3D polycrystalline perovskites, (ii) quasi-2D perovskites (Ruddlesden–Popper phase), and (iii) 0D perovskites (QDs). The low-dimensional quasi-2D and 0D perovskites in principle do not have the intrinsic limitations in EL efficiency originating from small exciton-binding energy and long exciton-diffusion length. On the contrary, the 3D MHPs have these intrinsic limitations in EL efficiency despite their strong advantages of easy synthesis and favorable optical and electrical properties for optoelectronics, as discussed previously. Therefore, efficient strategies to overcome these fundamental issues in 3D MHP emitters should be further developed. To improve the EL efficiency of 3D polycrystalline PeLEDs having a narrow FWHM ( $\leq 20$  nm) by enhancing radiative recombination rates, the grain size must be reduced to the exciton Bohr diameter (e.g.,  $\sim 10$  nm for MAPbBr<sub>3</sub>) to achieve effective spatial confinement of excitons in nanograins. Furthermore, the formation of perfect single-crystalline nanograins without bulk defects and the surface-defect passivation by semiconducting additives can be a promising strategy.

One way to achieve this goal is to mimic the core-shell system of low-dimensional MHPs, which are surrounded by bulky organic cations or insulating ligands (i.e., 3D MHP polycrystals surrounded by semiconducting organic additives),<sup>4,84,148</sup> to simultaneously overcome the limited charge transport in low-dimensional perovskites and the defective grain-boundary in 3D polycrystalline MHP films. Small nanograins surrounded by organic semiconducting additives will also reduce  $n_r$  of the 3D MHP films. This is because low- $n_r$  organic additives at the grain-boundary region can effectively separate the high- $n_r$  MHP nanograins, thereby reducing  $n_r$  of the 3D film as a whole. A low  $n_r$  can reduce the waveguide mode optical loss at the interface between the MHP emitting layer and the organic layers. The light outcoupling efficiency can then be maximized by simultaneously controlling the thickness of MHP emitting layers. Another possible approach to enhance LE of PeLED is to selectively increase the bimolecular recombination rate. Basically, LE of Pb-based MHPs is limited due to their inherently slow  $k_2 \approx 10^{-10}$  cm<sup>3</sup> s<sup>-1</sup>.<sup>37</sup> If we were able to increase  $k_2$  to  $>10^{-8}$  cm<sup>3</sup> s<sup>-1</sup> while maintaining  $k_1$  and  $k_3$ , we would obtain highly luminescent MHP crystals. Although MHPs that are characterized by these sorts of ideal recombination rates have not been reported yet,

we expect that MHPs based on other central metals such as Mn<sup>150</sup> and Bi<sup>151,152</sup> or partial doping of these into Pb could be promising candidates.

As discussed in Sec. II C, LE of MHPs can be enhanced by facilitating the radiative decay of charge carriers by suppressing the charge carrier–ionic lattice interactions such as the large polaron effect and hot-phonon bottleneck.<sup>60</sup> Because the hot-phonon bottleneck is boosted by the nonequilibrium LO-phonon population that can arise from the mass difference between each participating ions,<sup>64</sup> ions with similar masses must be used in MHP crystals to prevent the hot-phonon bottleneck. The hot-phonon bottleneck also could be originated from ferroelectric characteristics of MHPs which arise from the reorientation of OA (e.g., MA<sup>+</sup>) under the electric fields.<sup>64,153</sup> Therefore, MHPs without having the hot-phonon bottleneck as well as polaron effect should be developed to further improve the EL efficiency in PeLEDs by suppressing the charge carrier–ionic lattice interactions, thus, by facilitating the radiative recombination of electron–hole pairs.<sup>56</sup> In view of these, a novel nanostructure that simultaneously exhibits the spatial confinement of excitons and the suppressed charge carrier–ionic lattice interaction is highly desirable in the near future.

Finally, the strategies to improve EL efficiency in PeLEDs should be accompanied by improvement in the device lifetime. Possible influences on the device lifetime include the following: (i) effective charge balance, which possibly induces a uniform recombination throughout the MHP emitting layers and avoids a local charge accumulation that accelerates ion migration owing to a local electric field. (ii) A pinhole-free and smooth surface morphology can reduce the local leakage current that causes Joule heating and degrades the thermal stability. (iii) Defect passivation can effectively impede an ion migration at the grain-boundary region and improve chemical stability. Chemically stable MHP films can improve operational device lifetime. In particular, when small nanograins used to achieve high-efficiency 3D polycrystalline PeLEDs are inevitably accompanied by the high-density grain-boundary region, passivating the grain-boundary region is a promising strategy to simultaneously improve device lifetime by suppressing the migration of ionic species.

#### ACKNOWLEDGMENTS

This research was supported by the Research Resettlement Fund for the new faculty of Seoul National University. This research was supported by the National Research Foundation (NRF) grant funded by the Ministry of Science, ICT and Future Planning, Korea government (Grant No. NRF-2016R1A3B1908431). This research was also supported by the Creative Materials Discovery Program through the NRF (Grant No. 2018M3D1A1058536), and BK21PLUS SNU Materials Division for Educating Creative Global Leaders (21A201319 12052).

#### REFERENCES

- <sup>1</sup>Y.-H. Kim, H. Cho, and T.-W. Lee, *Proc. Natl. Acad. Sci. U. S. A.* **113**, 11694 (2016).
- <sup>2</sup>Z.-K. Tan, R. S. Moghaddam, M. L. Lai, P. Docampo, R. Higler, F. Deschler, M. Price, A. Sadhanala, L. M. Pazos, D. Credgington, F. Hanusch, T. Bein, H. J. Snaith, and R. H. Friend, *Nat. Nanotechnol.* **9**, 687 (2014).
- <sup>3</sup>Y.-H. Kim, H. Cho, J. H. Heo, T.-S. Kim, N. Myoung, C.-L. Lee, S. H. Im, and T.-W. Lee, *Adv. Mater.* **27**, 1248 (2015).

- <sup>4</sup>H. Cho, S.-H. Jeong, M.-H. Park, Y.-H. Kim, C. Wolf, C.-L. Lee, J. H. Heo, A. Sadhanala, N. Myoung, S. Yoo, S. H. Im, R. H. Friend, and T.-W. Lee, *Science* **350**, 1222 (2015).
- <sup>5</sup>Y.-H. Kim, J. S. Kim, and T.-W. Lee, *Adv. Mater.* **31**, 1804595 (2018).
- <sup>6</sup>B. Saparov and D. B. Mitzi, *Chem. Rev.* **116**, 4558 (2016).
- <sup>7</sup>C. Li, X. Lu, W. Ding, L. Feng, Y. Gao, and Z. Guo, *Acta Crystallogr., Sect. B: Struct. Sci.* **64**, 702 (2008).
- <sup>8</sup>W. Travis, E. N. K. Glover, H. Bronstein, D. O. Scanlon, and R. G. Palgrave, *Chem. Sci.* **7**, 4548 (2016).
- <sup>9</sup>M. Becker, T. Klüner, and M. Wark, *Dalton Trans.* **46**, 3500 (2017).
- <sup>10</sup>T. M. Brenner, D. A. Egger, L. Kronik, G. Hodes, and D. Cahen, *Nat. Rev. Mater.* **1**, 15007 (2016).
- <sup>11</sup>Z. Xiao, R. A. Kerner, L. Zhao, N. L. Tran, K. M. Lee, T.-W. Koh, G. D. Scholes, and B. P. Rand, *Nat. Photonics* **11**, 108 (2017).
- <sup>12</sup>H.-K. Seo, H. Kim, J. Lee, M.-H. Park, S.-H. Jeong, Y.-H. Kim, S.-J. Kwon, T.-H. Han, S. Yoo, and T.-W. Lee, *Adv. Mater.* **29**, 1605587 (2017).
- <sup>13</sup>M.-H. Park, S.-H. Jeong, H.-K. Seo, C. Wolf, Y.-H. Kim, H. Kim, J. Byun, J. S. Kim, H. Cho, and T.-W. Lee, *Nano Energy* **42**, 157 (2017).
- <sup>14</sup>L. Meng, E.-P. Yao, Z. Hong, H. Chen, P. Sun, Z. Yang, G. Li, and Y. Yang, *Adv. Mater.* **29**, 1603826 (2017).
- <sup>15</sup>Y. Shi, J. Xi, T. Lei, F. Yuan, J. Dai, C. Ran, H. Dong, B. Jiao, X. Hou, and Z. Wu, *ACS Appl. Mater. Interfaces* **10**, 9849 (2018).
- <sup>16</sup>K. Lin, J. King, L. N. Quan, F. P. G. deArquer, X. Gong, J. Lu, L. Xie, W. Zhao, D. Zhang, C. Yan, W. Li, X. Liu, Y. Lu, J. Kirman, E. H. Sargent, Q. Xiong, and Z. Wei, *Nature* **562**, 245 (2018).
- <sup>17</sup>Y. Cao, N. Wang, H. Tian, J. Guo, Y. Wei, H. Chen, Y. Miao, W. Zou, K. Pan, Y. He *et al.*, *Nature* **562**, 249 (2018).
- <sup>18</sup>P. Chen, Y. Meng, M. Ahmadi, Q. Peng, C. Gao, L. Xu, M. Shao, Z. Xiong, and B. Hu, *Nano Energy* **50**, 615 (2018).
- <sup>19</sup>X. Zhao, J. D. A. Ng, R. H. Friend, and Z.-K. Tan, *ACS Photonics* **5**, 3866 (2018).
- <sup>20</sup>Y. Toyozawa, *Optical Processes in Solids* (Cambridge University Press, Cambridge, UK, 2003), pp. 113–148.
- <sup>21</sup>S. Adjokatse, H.-H. Fang, and M. A. Loi, *Mater. Today* **20**, 413 (2017).
- <sup>22</sup>K. Tanaka, T. Takahashi, T. Ban, T. Kondo, K. Uchida, and N. Miura, *Solid State Commun.* **127**, 619 (2003).
- <sup>23</sup>I. B. Koutselas, L. Ducasse, and G. C. Papavassiliou, *J. Phys. Condens. Matter* **8**, 1217 (1996).
- <sup>24</sup>N. Sestu, M. Cadelano, V. Sarritsu, F. Chen, D. Marongiu, R. Piras, M. Mainas, F. Quochi, M. Saba, A. Mura, and G. Bongiovanni, *J. Phys. Chem. Lett.* **6**, 4566 (2015).
- <sup>25</sup>K. Wu, A. Bera, C. Ma, Y. Du, Y. Yang, L. Li, and T. Wu, *Phys. Chem. Chem. Phys.* **16**, 22476 (2014).
- <sup>26</sup>V. D'Innocenzo, G. Grancini, M. J. P. Alcocer, A. R. S. Kandada, S. D. Stranks, M. M. Lee, G. Lanzani, H. J. Snaith, and A. Petrozza, *Nat. Commun.* **5**, 3586 (2014).
- <sup>27</sup>J. Byun, H. Cho, C. Wolf, M. Jang, A. Sadhanala, R. H. Friend, H. Yang, and T.-W. Lee, *Adv. Mater.* **28**, 7515 (2016).
- <sup>28</sup>T. Ishihara, *J. Lumin.* **60–61**, 269 (1994).
- <sup>29</sup>Q. Lin, A. Armin, R. C. R. Nagiri, P. L. Burn, and P. Meredith, *Nat. Photonics* **9**, 106 (2015).
- <sup>30</sup>E. A. Muljarov, S. G. Tikhodeev, N. A. Gippius, and T. Ishihara, *Phys. Rev. B* **51**, 14370 (1995).
- <sup>31</sup>M. Shinada and S. Sugano, *J. Phys. Soc. Jpn.* **21**, 1936 (1966).
- <sup>32</sup>E. Hanamura, N. Nagaosa, M. Kumagai, and T. Takagahara, *Mater. Sci. Eng. B* **1**, 255 (1988).
- <sup>33</sup>D. B. Tran Thoai, R. Zimmermann, M. Grundmann, and D. Bimberg, *Phys. Rev. B* **42**, 5906 (1990).
- <sup>34</sup>X. Hong, T. Ishihara, and A. V. Nurmikko, *Phys. Rev. B* **45**, 6961 (1992).
- <sup>35</sup>H. Takagi, H. Kunugita, and K. Ema, *Phys. Rev. B* **87**, 125421 (2013).
- <sup>36</sup>X. Hong, T. Ishihara, and A. V. Nurmikko, *Solid State Commun.* **84**, 657 (1992).
- <sup>37</sup>G. Xing, B. Wu, X. Wu, M. Li, B. Du, Q. Wei, J. Guo, E. K. L. Yeow, T. C. Sum, and W. Huang, *Nat. Commun.* **8**, 14558 (2017).
- <sup>38</sup>Y. Yang, M. Yang, Z. Li, R. Crisp, K. Zhu, and M. C. Beard, *J. Phys. Chem. Lett.* **6**, 4688 (2015).
- <sup>39</sup>S. D. Stranks, V. M. Burlakov, T. Leijtens, J. M. Ball, A. Goriely, and H. J. Snaith, *Phys. Rev. Appl.* **2**, 034007 (2014).
- <sup>40</sup>J. M. Richter, M. Abdi-Jalebi, A. Sadhanala, M. Tabachnyk, J. P. H. Rivett, L. M. Pazos-Outón, K. C. Gödel, M. Price, F. Deschler, and R. H. Friend, *Nat. Commun.* **7**, 13941 (2016).
- <sup>41</sup>C. Wehrenfennig, M. Z. Liu, H. J. Snaith, M. B. Johnston, and L. M. Herz, *Energy Environ. Sci.* **7**, 2269 (2014).
- <sup>42</sup>Y. Yamada, T. Nakamura, M. Endo, A. Wakamiya, and Y. Kanemitsu, *J. Am. Chem. Soc.* **136**, 11610 (2014).
- <sup>43</sup>M. Yuan, L. N. Quan, R. Comin, G. Walters, R. Sabatini, O. Voznyy, S. Hoogland, Y. Zhao, E. M. Beauregard, P. Kanjanaboos, Z. Lu, D. H. Kim, and E. H. Sargent, *Nat. Nanotechnol.* **11**, 872 (2016).
- <sup>44</sup>N. Wang, L. Cheng, R. Ge, S. Zhang, Y. Miao, W. Zou, C. Yi, Y. Sun, Y. Cao, R. Yang *et al.*, *Nat. Photonics* **10**, 699 (2016).
- <sup>45</sup>X. Yang, X. Zhang, J. Deng, Z. Chu, Q. Jiang, J. Meng, P. Wang, L. Zhang, Z. Yin, and J. You, *Nat. Commun.* **9**, 1169 (2018).
- <sup>46</sup>H. Kim, J. S. Kim, J.-M. Heo, M. Pei, L.-H. Park, Z. Liu, H. J. Yun, M.-H. Park, S.-H. Jeong, Y.-H. Kim, J.-W. Park, L. Zhang, H. yang, H. M. Jang, K. P. Loh, N.-G. Park, and T. W. Lee, "Proton-transfer induced 3D/2D hybrid perovskite for stable light-emitting diodes," *Nat. Commun.* (unpublished).
- <sup>47</sup>T. Shi, W. Yin, F. Hong, K. Zhu, and Y. Yan, *Appl. Phys. Lett.* **106**, 103902 (2015).
- <sup>48</sup>W.-J. Yin, T. Shi, and Y. Yan, *Appl. Phys. Lett.* **104**, 063903 (2014).
- <sup>49</sup>M. Sebastian, J. A. Peters, C. C. Stoumpos, J. Im, S. S. Kostina, Z. Liu, M. G. Kanatzidis, A. J. Freeman, and B. W. Wessels, *Phys. Rev. B* **92**, 235210 (2015).
- <sup>50</sup>A. R. S. Kandada and A. Petrozza, *APL Mater.* **4**, 091506 (2016).
- <sup>51</sup>F. Zheng, L. Z. Tan, S. Liu, and A. M. Rappe, *Nano Lett.* **15**, 7794 (2015).
- <sup>52</sup>T. Etinne, E. Mosconi, and F. De Angelis, *J. Phys. Chem. Lett.* **7**, 1638 (2016).
- <sup>53</sup>X. Zhang, J.-X. Shen, and C. G. Van de Walle, *J. Phys. Chem. Lett.* **9**, 2903 (2018).
- <sup>54</sup>C. Motta, F. El-Mellouhi, S. Kais, N. Tabet, F. Alharbi, and S. Sanvito, *Nat. Commun.* **6**, 7026 (2014).
- <sup>55</sup>I. P. Swainson, C. Stock, S. F. Parker, L. Van Eijck, M. Russina, and J. W. Taylor, *Phys. Rev. B* **92**, 100303 (2015).
- <sup>56</sup>H. Zhu, K. Miyata, Y. Fu, J. Wang, P. P. Joshi, D. Niesner, K. W. Williams, S. Jin, and X.-Y. Zhu, *Science* **353**, 1409 (2016).
- <sup>57</sup>X.-Y. Zhu and V. Podzorov, *J. Phys. Chem. Lett.* **6**, 4758 (2015).
- <sup>58</sup>K. Miyata, T. L. Atallah, and X.-Y. Zhu, *Sci. Adv.* **3**, e1701469 (2017).
- <sup>59</sup>J. M. Frost and A. Walsh, *Acc. Chem. Res.* **49**, 528 (2016).
- <sup>60</sup>K. Miyata, D. Meggiolaro, M. T. Trinh, P. P. Joshi, E. Mosconi, S. C. Jones, F. De Angelis, and X.-Y. Zhu, *Sci. Adv.* **3**, e1701217 (2017).
- <sup>61</sup>H. Zhu, M. T. Trinh, J. Wang, Y. Fu, P. P. Joshi, K. Miyata, S. Jin, and X.-Y. Zhu, *Adv. Mater.* **29**, 1603072 (2017).
- <sup>62</sup>Y. Rosenwaks, M. C. Hanna, D. H. Levi, D. M. Szymd, R. K. Ahrenkiel, and A. J. Nozik, *Phys. Rev. B* **48**, 14675 (1993).
- <sup>63</sup>M. B. Price, J. Butkus, T. C. Jellicoe, A. Sadhanala, A. Briane, J. E. Halpert, K. Broch, J. M. Hodgkiss, R. H. Friend, and F. Deschler, *Nat. Commun.* **6**, 8420 (2015).
- <sup>64</sup>Y. Yang, D. P. Ostrowski, R. M. France, K. Zhu, J. Van De Lagemaat, J. M. Luther, and M. C. Beard, *Nat. Photonics* **10**, 53 (2016).
- <sup>65</sup>F. M. Peters and J. T. Devreese, *Phys. Rev. B* **31**, 4890 (1985).
- <sup>66</sup>M. Sendner, P. K. Nayak, D. A. Egger, S. Beck, C. Meller, B. Epping, W. Kowalsky, L. Kronik, H. J. Snaith, A. Pucci, and R. Lovrincic, *Mater. Horiz.* **3**, 613 (2016).
- <sup>67</sup>K. Chen, A. J. Barker, F. L. C. Morgan, J. E. Halpert, and J. M. Hodgkiss, *J. Phys. Chem. Lett.* **6**, 153 (2015).
- <sup>68</sup>A. D. Wright, C. Verdi, R. L. Milot, G. E. Eperon, M. A. Pérez-Osorio, H. J. Snaith, F. Giustino, M. B. Johnston, and L. M. Herz, *Nat. Commun.* **7**, 11755 (2016).
- <sup>69</sup>D. W. de Quilettes, S. M. Vorpahl, S. D. Stranks, H. Nagaoka, G. E. Eperon, M. E. Ziffer, H. J. Snaith, and D. S. Ginger, *Science* **348**, 683 (2015).
- <sup>70</sup>S.-H. Wei, *Comput. Mater. Sci.* **30**, 337 (2004).
- <sup>71</sup>Y. Huang, W.-J. Yin, and Y. He, *J. Phys. Chem. C* **122**, 1345 (2018).
- <sup>72</sup>W.-J. Yin, T. Shi, and Y. Yan, *Adv. Mater.* **26**, 4653 (2014).

- <sup>73</sup>F. Zhang, H. Zhong, C. Chen, X. Wu, X. Hu, H. Huang, J. Han, B. Zou, and Y. Dong, *ACS Nano* **9**, 4533 (2015).
- <sup>74</sup>L. Protesescu, S. Yakunin, M. I. Bodnarchuk, F. Krieg, R. Caputo, C. H. Hendon, R. X. Yang, A. Walsh, and M. V. Kovalenko, *Nano Lett.* **15**, 3692 (2015).
- <sup>75</sup>G. Xing, N. Mathews, S. S. Lim, N. Yantara, X. Liu, D. Sabba, M. Grätzel, S. Mhaisalkar, and T. C. Sum, *Nat. Mater.* **13**, 476 (2014).
- <sup>76</sup>L. Wang, C. McCleese, A. Kovalsky, Y. Zhao, and C. Burda, *J. Am. Chem. Soc.* **136**, 12205 (2014).
- <sup>77</sup>Y. Yuan and J. Huang, *Acc. Chem. Res.* **49**, 286 (2016).
- <sup>78</sup>L. Zhao, J. Gao, Y. L. Lin, Y.-W. Yeh, K. M. Lee, N. Yao, Y.-L. Loo, and B. P. Rand, *Adv. Mater.* **29**, 1605317 (2017).
- <sup>79</sup>L. Zhao, Y.-W. Yeh, N. L. Tran, F. Wu, Z. Xiao, R. A. Kerner, Y. L. Lin, G. D. Scholes, N. Yao, and B. P. Rand, *ACS Nano* **11**, 3957 (2017).
- <sup>80</sup>Y. Lin, Y. Bai, Y. Fang, Q. Wang, Y. Deng, and J. Huang, *ACS Energy Lett.* **2**, 1571 (2017).
- <sup>81</sup>C. Eames, J. M. Frost, P. R. F. Barnes, B. C. O'Regan, A. Walsh, and M. S. Islam, *Nat. Commun.* **6**, 7497 (2015).
- <sup>82</sup>W. Tress, N. Marinova, T. Moehl, S. M. Zakeeruddin, M. K. Nazeeruddin, and M. Grätzel, *Energy Environ. Sci.* **8**, 995 (2015).
- <sup>83</sup>J. S. Yun, J. Seidel, J. Kim, A. M. Soufiani, S. Huang, J. Lou, N. J. Jeon, S. I. Seok, M. A. Green, and A. Ho-Baillie, *Adv. Energy Mater.* **6**, 1600330 (2016).
- <sup>84</sup>M.-H. Park, J. Park, J. Lee, H. S. So, H. Kim, S.-H. Jeong, T.-H. Han, C. Wolf, H. Lee, S. Yoo, and T. W. Lee, *Adv. Funct. Mater.* **29**, 1902017 (2019).
- <sup>85</sup>J. Singh, in *Quantum Mechanics. Fundamentals and Applications to Technology* (John Wiley & Sons, 1997), Chap. 9.
- <sup>86</sup>J. Sakurai, in *Modern Quantum Mechanics*, Revised ed., edited by S. F. Tuan (Addition-Wesley Pub. Co., 1994), Chap. 5.
- <sup>87</sup>J.-H. Lee, N. C. Bristowe, J. H. Lee, S.-H. Lee, P. D. Bristowe, A. K. Cheetham, and H. M. Jang, *Chem. Mater.* **28**, 4259 (2016).
- <sup>88</sup>D. Kim, H. Han, J. H. Lee, J. W. Choi, J. C. Grossman, H. M. Jang, and D. Kim, *Proc. Natl. Acad. Sci. U. S. A.* **115**, 6566 (2018).
- <sup>89</sup>J. H. Lee, J.-H. Lee, E.-H. Kong, and H. M. Jang, *Sci. Reports* **6**, 21687 (2016).
- <sup>90</sup>K. Zheng, Q. Zhu, M. Abdellah, M. E. Messing, W. Zhang, A. Generalov, Y. Niu, L. Ribaud, S. E. Canton, and T. Pullerits, *J. Phys. Chem. Lett.* **6**, 2969 (2015).
- <sup>91</sup>L. C. Schmidt, A. Pertegás, S. González-Carrero, O. Malinkiewicz, S. Agouram, G. M. Espallargas, H. J. Bolink, R. F. Galian, and J. Pérez-Prieto, *J. Am. Chem. Soc.* **136**, 850 (2014).
- <sup>92</sup>Y. Kim, E. Yassitepe, O. Voznyy, R. Comin, G. Walters, X. Gong, P. Kanjanaboos, A. F. Nogueira, and E. H. Sargent, *ACS Appl. Mater. Interfaces* **7**, 25007 (2015).
- <sup>93</sup>D. M. Jang, K. Park, D. H. Kim, J. Park, F. Shojaei, H. S. Kang, J.-P. Ahn, J. W. Lee, and J. K. Song, *Nano Lett.* **15**, 5191 (2015).
- <sup>94</sup>P. O. Anikeeva, J. E. Halpert, M. G. Bawendi, and V. Bulović, *Nano Lett.* **9**, 2532 (2009).
- <sup>95</sup>Y. Kayanuma, *Solid State Commun.* **59**, 405 (1986).
- <sup>96</sup>Y. Kayanuma, *Phys. Rev. B* **38**, 9797 (1988).
- <sup>97</sup>G. T. Einevoll, *Phys. Rev. B* **45**, 3410 (1992).
- <sup>98</sup>L. E. Brus, *J. Chem. Phys.* **80**, 4403 (1984).
- <sup>99</sup>Y.-H. Kim, C. Wolf, Y.-T. Kim, H. Cho, W. Kwon, S. Do, A. Sadhanala, C. G. Park, S.-W. Rhee, S. H. Im, R. H. Friend, and T.-W. Lee, *ACS Nano* **11**, 6586 (2017).
- <sup>100</sup>G. Ma, S.-H. Tang, W. Sun, Z. Shen, W. Huang, and J. Shi, *Phys. Lett. A* **299**, 581 (2002).
- <sup>101</sup>T. Tachikawa, I. Karimata, and Y. Kobori, *J. Phys. Chem. Lett.* **6**, 3195 (2015).
- <sup>102</sup>Y.-K. Chih, J.-C. Wang, R.-T. Yang, C.-C. Liu, Y.-C. Chang, Y.-S. Fu, W.-C. Lai, P. Chen, T.-C. Wen, Y.-C. Huang *et al.*, *Adv. Mater.* **28**, 8687 (2016).
- <sup>103</sup>J. C. Yu, D. W. Kim, D. Bin Kim, E. D. Jung, K.-S. Lee, S. Lee, D. Di Nuzzo, J.-S. Kim, and M. H. Song, *Nanoscale* **9**, 2088 (2017).
- <sup>104</sup>M. Xiao, F. Huang, W. Huang, Y. Dkhissi, Y. Zhu, J. Etheridge, A. Gray-Weale, U. Bach, Y.-B. Cheng, and L. Spiccia, *Angew. Chem.* **126**, 10056 (2014).
- <sup>105</sup>N. Kawano, M. Koshimizu, Y. Sun, N. Yahaba, Y. Fujimoto, T. Yanagida, and K. Asai, *J. Phys. Chem.* **118**, 9101 (2014).
- <sup>106</sup>Z. Chen, C. Zhang, X.-F. Jiang, M. Liu, R. Xia, T. Shi, D. Chen, Q. Xue, Y.-J. Zhao, S. Su, H.-L. Yip, and Y. Cao, *Adv. Mater.* **29**, 1603157 (2017).
- <sup>107</sup>J. Song, J. Li, X. Li, L. Xu, Y. Dong, and H. Zeng, *Adv. Mater.* **27**, 7162 (2015).
- <sup>108</sup>W. Deng, X. Xu, X. Zhang, Y. Zhang, X. Jin, L. Wang, S.-T. Lee, and J. Jie, *Adv. Funct. Mater.* **26**, 4797 (2016).
- <sup>109</sup>Y.-H. Kim, G.-H. Lee, Y.-T. Kim, C. Wolf, H. J. Yun, W. Kwon, C. G. Park, and T.-W. Lee, *Nano Energy* **38**, 51 (2017).
- <sup>110</sup>S. Kumar, J. Jagielski, N. Kallikounis, Y.-H. Kim, C. Wolf, F. Jenny, T. Tian, C. J. Hofer, Y.-C. Chiu, W. J. Stark, T.-W. Lee, and C.-J. Shih, *Nano Lett.* **17**, 5277 (2017).
- <sup>111</sup>G. Li, F. W. R. Rivarola, N. J. L. K. Davis, S. Bai, T. C. Jellicoe, F. De La Pena, S. Hou, C. Ducati, F. Gao, R. H. Friend, N. C. Greenham, and Z.-K. Tan, *Adv. Mater.* **28**, 3528 (2016).
- <sup>112</sup>H. Sun, Z. Yang, M. Wei, W. Sun, X. Li, S. Ye, Y. Zhao, H. Tan, E. L. Kynaston, T. B. Schon, H. Yan, Z.-H. Lu, G. A. Ozin, E. H. Sargent, and D. S. Seferos, *Adv. Mater.* **29**, 1701153 (2017).
- <sup>113</sup>F. Palazon, Q. A. Akkerman, M. Prato, and L. Manna, *ACS Nano* **10**, 1224 (2016).
- <sup>114</sup>J. Pan, L. N. Quan, Y. Zhao, W. Peng, B. Murali, S. P. Sarmah, M. Yuan, L. Sinatra, N. M. Alyami, J. Liu *et al.*, *Adv. Mater.* **28**, 8718 (2016).
- <sup>115</sup>J. Li, L. Xu, T. Wang, J. Song, J. Chen, J. Xue, Y. Dong, B. Cai, Q. Shan, B. Han, and H. Zeng, *Adv. Mater.* **29**, 1603885 (2017).
- <sup>116</sup>T. Chiba, K. Hoshi, Y.-J. Pu, Y. Takeda, Y. Hayashi, S. Ohisa, S. Kawata, and J. Kido, *ACS Appl. Mater. Interfaces* **9**, 18054 (2017).
- <sup>117</sup>T. Chiba, Y. Hayashi, H. Ebe, K. Hoshi, J. Sato, S. Sato, Y.-J. Pu, S. Ohisa, and J. Kido, *Nat. Photonics* **12**, 681 (2018).
- <sup>118</sup>I. L. Braly, D. W. DeQuilettes, L. M. Pazos-Outón, S. Burke, M. E. Ziffer, D. S. Ginger, and H. W. Hillhouse, *Nat. Photonics* **12**, 355 (2018).
- <sup>119</sup>L. Zhao, K. M. Lee, K. Roh, S. U. Z. Khan, and B. P. Rand, *Adv. Mater.* **31**, 1805836 (2019).
- <sup>120</sup>X.-B. Shi, Y. Liu, Z. Yuan, X.-K. Liu, Y. Miao, J. Wang, S. Lenk, S. Reineke, and F. Gao, *Adv. Opt. Mater.* **6**, 1800667 (2018).
- <sup>121</sup>M.-H. Park, J. S. Kim, J.-M. Heo, S. Ahn, S.-H. Jeong, and T.-W. Lee, *ACS Energy Lett.* **4**, 1134 (2019).
- <sup>122</sup>A. Vincent, S. Babu, E. Brinley, A. Karakoti, S. Deshpande, and S. Seal, *J. Phys. Chem. C* **111**, 8291 (2007).
- <sup>123</sup>S. Yu, T. K. S. Wong, K. Pita, and X. Hu, *J. Vac. Sci. Technol., B* **20**, 2036 (2002).
- <sup>124</sup>K.-M. Chiang, B.-W. Hsu, Y.-A. Chang, L. Yang, W.-L. Tsai, and H.-W. Lin, *ACS Appl. Mater. Interfaces* **9**, 040516 (2017).
- <sup>125</sup>J. Almutlaq, J. Yin, O. F. Mohammed, and O. M. Bakr, *J. Phys. Chem. Lett.* **9**, 4131 (2018).
- <sup>126</sup>S. Kumar, J. Jagielski, S. Yakunin, P. Rice, Y.-C. Chiu, M. Wang, G. Nedelcu, Y. Kim, S. Lin, E. J. G. Santos *et al.*, *ACS Nano* **10**, 9720 (2016).
- <sup>127</sup>T. C. Sum and N. Mathews, *Energy Environ. Sci.* **7**, 2518 (2014).
- <sup>128</sup>Q. Shan, J. Song, Y. Zou, J. Li, L. Xu, J. Xue, Y. Dong, B. Han, J. Chen, and H. Zeng, *Small* **13**, 1701770 (2017).
- <sup>129</sup>J. S. Yun, A. Ho-Baillie, S. Huang, S. H. Woo, Y. Heo, J. Seidel, F. Huang, Y.-B. Cheng, and M. A. Green, *J. Phys. Chem. Lett.* **6**, 875 (2015).
- <sup>130</sup>Z. Wang, F. Wang, W. Sun, R. Ni, S. Hu, J. Liu, B. Zhang, A. Alsaed, T. Hayat, and Z. Tan, *Adv. Funct. Mater.* **28**, 1804187 (2018).
- <sup>131</sup>S.-Y. Kim, W.-I. Jeong, C. Mayr, Y. S. Park, K.-H. Kim, J.-H. Lee, C.-K. Moon, W. Brütting, and J.-J. Kim, *Adv. Funct. Mater.* **23**, 3896 (2013).
- <sup>132</sup>M. J. Jurow, C. Mayr, T. D. Schmidt, T. Lampe, P. I. Djurovich, W. Brütting, and M. E. Thompson, *Nat. Mater.* **15**, 85 (2016).
- <sup>133</sup>J. P. H. Rivett, L. Z. Tan, M. B. Price, S. A. Bourelle, N. J. L. K. Davis, J. Xiao, Y. Zou, R. Middleton, B. Sun, A. M. Rappe, D. Credgington, and F. Deschler, *Nat. Commun.* **9**, 3531 (2018).
- <sup>134</sup>M. J. Jurow, T. Morgenstern, C. Eisler, J. Kang, E. Penzo, M. Do, M. Engel-mayer, W. T. Osowiecki, Y. Bekenstein, C. Tossoni, L.-W. Wang, A. P. Alivisatos, W. Brütting, and Y. Liu, *Nano Lett.* **19**, 2489 (2019).
- <sup>135</sup>M. Lai, A. Obliger, D. Lu, C. S. Kley, C. G. Bischak, Q. Kong, T. Lei, L. Dou, N. S. Ginsberg, D. T. Limmer *et al.*, *Proc. Natl. Acad. Sci. U. S. A.* **115**, 11929 (2018).
- <sup>136</sup>W. Li, Y.-Y. Sun, L. Li, Z. Zhou, J. Tang, and O. V. Prezhdo, *J. Am. Chem. Soc.* **140**, 15753 (2018).
- <sup>137</sup>J.-W. Lee, Y. Choi, J. Yang, S. Ham, S. K. Jeon, J. Y. Lee, Y. Song, E. K. Ji, D. Yoon, S. Seo *et al.*, *ACS Nano* **11**, 3311 (2017).

- <sup>138</sup>D. E. Markov and P. W. M. Blom, *Phys. Rev. B* **72**, 161401 (2005).
- <sup>139</sup>F. Meng, C. Zhang, D. Chen, W. Zhu, H.-L. Yip, and S.-J. Su, *J. Mater. Chem. C* **5**, 6169 (2017).
- <sup>140</sup>M. Abdi-Jalebi, Z. Andaji-Garmaroudi, S. Cacovich, C. Stavrakas, B. Philippe, J. M. Richter, M. Alsari, E. P. Booker, E. M. Hutter, A. J. Pearson *et al.*, *Nature* **555**, 497 (2018).
- <sup>141</sup>M. Saliba, T. Matsui, J.-Y. Seo, K. Domanski, J.-P. Correa-Baena, M. K. Nazeeruddin, S. M. Zakeeruddin, W. Tress, A. Abate, A. Hagfeldt *et al.*, *Energy Environ. Sci.* **9**, 1989 (2016).
- <sup>142</sup>H. Cho, J. S. Kim, C. Wolf, Y.-H. Kim, H. J. Yun, S.-H. Jeong, A. Sadhanala, V. Venugopalan, J. W. Choi, C.-L. Lee *et al.*, *ACS Nano* **12**, 2883 (2018).
- <sup>143</sup>M. I. Saidaminov, J. Kim, A. Jain, R. Quintero-Bermudez, H. Tan, G. Long, F. Tan, A. Johnston, Y. Zhao, O. Voznyy *et al.*, *Nat. Energy* **3**, 648 (2018).
- <sup>144</sup>C. H. Seager, *Annu. Rev. Mater. Sci.* **15**, 271 (1985).
- <sup>145</sup>Y. Liu, K. Palotas, X. Yuan, T. Hou, H. Lin, Y. Li, and S.-T. Lee, *ACS Nano* **11**, 2060 (2017).
- <sup>146</sup>H. Uratani and K. Yamashita, *J. Phys. Chem. Lett.* **8**, 742 (2017).
- <sup>147</sup>N. K. Noel, A. Abate, S. D. Stranks, E. S. Parrott, V. M. Burlakov, A. Goriely, and H. J. Snaith, *ACS Nano* **8**, 9815 (2014).
- <sup>148</sup>D. W. de Quilettes, S. Koch, S. Burke, R. K. Paranji, A. J. Shropshire, M. E. Ziffer, and D. S. Ginger, *ACS Energy Lett.* **1**, 438 (2016).
- <sup>149</sup>L. Song, X. Guo, Y. Hu, Y. Lv, J. Lin, Z. Liu, Y. Fan, and X. Liu, *J. Phys. Chem. Lett.* **8**, 4148 (2017).
- <sup>150</sup>S. Zou, Y. Liu, J. Li, C. Liu, R. Feng, F. Jiang, Y. Li, J. Song, H. Zeng, M. Hong, and X. Chen, *J. Am. Chem. Soc.* **139**, 11443 (2017).
- <sup>151</sup>Y. Zhou, Z.-J. Yong, K.-C. Zhang, B.-M. Liu, Z.-W. Wang, J.-S. Hou, Y.-Z. Fang, Y. Zhou, H.-T. Sun, and B. Song, *J. Phys. Chem. Lett.* **7**, 2735 (2016).
- <sup>152</sup>R. Begum, M. R. Parida, A. L. Abdelhady, B. Murali, N. M. Alyami, G. H. Ahmed, M. N. Hedhili, O. M. Bakr, and O. F. Mohammed, *J. Am. Chem. Soc.* **139**, 731 (2017).
- <sup>153</sup>C. C. Stoumpos, C. D. Malliakas, and M. G. Kanatzidis, *Inorg. Chem.* **52**, 9019 (2013).